Nature of the Stratospheric Haze on Uranus: Evidence for Condensed Hydrocarbons

James B. Pollack,[1] Kathy Rages,[1] Shelly K. Pope,[2] Martin G. Tomasko,[2] Paul N. Romani,[3] and Sushil K. Atreya[4]

We have used a number of models to analyze Voyager images of Uranus obtained at several high phase angles to derive physical and chemical properties of particulate matter present in the planet's lower stratosphere. These models include a multiple-scattering algorithm for plane parallel atmospheres, a spherical atmosphere code for performing limb inversions, a microphysical model of aerosol formation, growth, and sedimentation, and a photochemical model of methane photolysis. We obtain definitive evidence for the presence of aerosols at pressure levels ranging from a few millibars to about 100 mbar. There are two possible sets of particle properties that can fit radiances observed close to but somewhat interior to the limb at several phase angles in four visible wavelength bands. The low-density solution is characterized by particles having a modal radius and number density equal to 0.13 ± 0.02 μm and 2 ± 1 particles/cm^3, respectively, at a pressure level of 44 mbar. The alternative, high-density solution is characterized by particles having a modal radius that is 0.6–0.7 times that of the low-density solution at the reference level and a density that is 2 orders of magnitude larger. Since the high-density solution implies a mass production rate for the stratospheric aerosols that is much larger than those that can plausibly be supplied by photochemically produced gases that condense, whereas the low-density solution does not, we favor the low-density solution. Inversion of narrow-angle, high-resolution images of the limb provides a definition of a variable that provides a measure of the amount of aerosol scattering at high phase angles. The vertical profile of this variable shows a decrease of several orders of magnitude from pressure levels of tens to a few millibars. This decrease is due chiefly to the particle size of the aerosols becoming small compared to a wavelength. Above the base of the stratosphere the aerosol optical depth is approximately 0.01 in the mid-visible. A major source for the stratospheric aerosols is the condensation of ethane, acetylene, and diacetylene gas species at pressure levels of approximately 14, 2.5, and 0.1 mbar, respectively. These gases are produced at much higher altitudes by solar UV photolysis of methane and diffuse to the lower stratosphere, where they condense. In addition, diacetylene is also produced photochemically within its condensation region. Condensation of locally produced diacetylene may represent a significant fraction of the total hydrocarbon condensation. Such a local source of condensation may be required by the inversions to the limb profiles, which indicate that at least half of the ice condensation occurs at altitudes above the 5-mbar level. The hypothesis that the stratospheric particles are made of hydrocarbon ices is supported by the approximate agreement between the total ice condensation rate predicted by the methane photochemical model and the aerosol mass production rate derived for the low-density solution of the Voyager data. The aerosol mass production rate derived from the Voyager data is equal to $2–15 \times 10^{-17}$ g/cm^2/s. Additional but weaker support for this hypothesis is provided by the Voyager radio occultation temperature profiles. It is suggested that solar UV radiation promotes solid state chemistry within the lower order hydrocarbon ices, resulting in the production of polymers capable of absorbing at visible wavelengths. Thus this altered material could play a key role in the planet's heat budget. Ethane, acetylene, and diacetylene ices evaporate at approximately the 600-, 900-, and 3000-mbar levels of the upper troposphere. The polymeric material is expected to evaporate at pressures in excess of the evaporation level for diacetylene.

1. Introduction

Photochemical hazes are present in the upper tropospheres and lower stratospheres of a number of planets and satellites. They are the end products of solar UV radiation and energetic particles acting on atmospheric gases. The products of the resultant chemical transformations include molecules more complicated than the starting gases, which condense at ambient temperatures to form submicron-sized particles. Examples of such hazes include sulfuric acid particles present in Earth's stratosphere and Venus' upper troposphere, which are generated from sulfur-containing gases; complicated H,C,N-containing hazes of Titan's upper atmosphere, which are produced from CH_4 and N_2; and hazes of unknown composition in Jupiter's and Saturn's stratospheres, which are manufac-

tured from CH_4, NH_3, and/or PH_3 [*Toon and Farlow*, 1981; *Esposito et al.*, 1983; *Rages et al.*, 1983; *Atreya and Romani*, 1985; *Smith and Tomasko*, 1984; *Tomasko and Doose*, 1984; *West et al.*, 1986].

The production of a photochemical haze in Uranus' stratosphere may be a more well-constrained situation than is the case for Jupiter's and Saturn's stratospheres. Temperatures are so low near the Uranian tropopause ($\simeq 50–55$ K) [*Tyler et al.*, 1986] that CH_4 is perhaps the only gas present in large enough amounts in the Uranian stratosphere to be capable of producing haze particles. Furthermore, temperatures are cold enough in the lower stratosphere [*Tyler et al.*, 1986] that simple photochemical products of methane photolysis, such as ethane and acetylene, are capable of condensing there [*Atreya and Ponthreu*, 1983; *Atreya and Romani*, 1985]. Thus it may be possible to predict the composition and production levels of photochemical hazes in the Uranian stratosphere.

Determinations of the occurrence and properties of a haze in Uranus' stratosphere are important for improving our understanding of the photochemistry of its upper atmosphere and for constraining the properties of a potentially important contributor to the radiative heating of the lower stratosphere and upper troposphere. These properties will also set the stage for obtaining a precise estimate of the planet's bolometric

[1]NASA Ames Research Center, Moffett Field, California.
[2]University of Arizona, Tucson.
[3]NASA Goddard Space Flight Center, Greenbelt, Maryland.
[4]University of Michigan, Ann Arbor.

albedo and, thus, aid in evaluating the magnitude of the planet's relatively weak internal heat source.

Up until recently, there has been marginal evidence for the presence of stratospheric hazes on Uranus. In principal, measurements of the planet's long-wavelength UV spectrum can uniquely detect these particles if they absorb at UV wavelengths, since molecular Rayleigh scattering limits the penetration of long-wavelength solar UV radiation to levels in the lower stratosphere. Unfortunately, such a detection has proved to be difficult owing to uncertainties in the solar UV spectrum and the limited amount of absorbing haze particles. Using solar analog stars to calibrate UV spectra taken from the International Ultraviolet Explorer (IUE) spacecraft, *Wagener et al.* [1986] inferred a UV reflectivity spectrum that lay close to that expected from only molecular Rayleigh and Raman scattering. Using the same Δ spectra but calibrating them with nonsynchronous rocket spectra of the Sun, J. S. Neff et al. (unpublished work, 1987) concluded that Uranus' UV reflectivity was less than that expected from just molecular scattering. If so, absorbing haze material must be present in the planet's stratosphere.

In contrast to the situation at UV wavelengths the well-alibrated reflectivity spectrum of Uranus obtained by *Neff et al.* [1984] for the 0.35- to 1.05-μm region provides unambiguous evidence for the presence of an absorbing aerosol [*Baines and Bergstralh*, 1986; *Pollack et al.*, 1986a, b]. Unfortunately, it is not possible to determine the precise location of this aerosol from these low phase angle, disk-integrated data. In particular, it is not possible to determine whether these particles are present only in the upper troposphere, only in the lower stratosphere, or both.

Observations of Uranus from the Voyager 2 spacecraft with the visible imaging camera [*Smith et al.*, 1986] and photopolarimeter (PPS) experiment [*Lane et al.*, 1986] provide the critical data needed both to detect and characterize the stratospheric haze of Uranus. These observations encompass a wide range of phase angles, including very high ones, resolve the disk of the planet (both instruments) as well as its limb (only the camera), and provide broad band photometry at a number of visible wavelengths (the camera) as well as at a near UV and a near IR wavelength (the photopolarimeter). Very preliminary analyses of the imaging data provide strong evidence for the presence of a stratospheric haze and a crude estimate of the mean particle size (a few tenths of a micron) [*Smith et al.*, 1986]. The former conclusion was supported by very preliminary analysis of low phase angle, disk-resolved scans taken with the near UV channel of PPS [*Lane et al.*, 1986].

In this paper we report the results of an in-depth analysis of Voyager imaging data directed at confirming the presence and determining the physical and chemical characteristics of the Uranian stratospheric haze. We focus on data taken at high phase angles, since the observed radiances are determined almost entirely by scattering occurring in the stratosphere. This data set includes images taken at several phase angles through a number of filters of the wide-angle camera, which permit an estimate of the relative contribution of molecules and aerosols to the observed brightnesses and a determination of the mean size and optical depth of the haze, and images taken of the limb at several phase angles and several filters with the narrow-angle camera that provide vertical profiles with spatial resolutions better than an atmospheric scale height. We carry out the analyses of the Voyager imaging radiances with several radiative transfer programs, including one that takes account of the spherical geometry at the limb.

Important complements to the above analyses are provided by two sets of theoretical calculations. They involve modeling the photochemistry of the upper atmosphere and the microphysical processes that control the aerosols' properties. The photochemical calculations provide a definition of the composition, production levels, and production rates of hydrocarbon condensates in the stratosphere. Given the first two pieces of information from the photochemical model, the aerosol microphysical model can predict the size distribution and extinction coefficient of the haze as a function of altitude for various assumed parameters, most especially the aerosol production rate. Comparison of the predictions of the microphysical model with radiative transfer simulations of the imaging data constrains these parameters. The adequacy of both models, but especially the photochemical predictions, can be judged by comparing the two independent estimates of the aerosol production rate and by evaluating the degree of agreement between the predicted vertical profile and other aerosol properties and constraints placed by the data.

Below we successively describe the Voyager imaging data and its reduction, radiative transfer programs used to simulate and analyze this data, the photochemical model, and the aerosol microphysical model. Then, we report the results of our analyses at a latitude of approximately 20° in which we employ information from the two models to constrain our radiative transfer calculations and to test the quality of their predictions. Following this section, we discuss a number of issues involving the stratospheric aerosols, including characteristic time scales for their formation and loss, their possible partial evaporation in the upper troposphere, and their ability to provide absorption at visible wavelengths. In the final section, we summarize our principal conclusions.

2. PROCEDURE

In this section we describe our data reduction protocols and the models used to interpret the Voyager observations.

2.1. Voyager Data

At times of approximately 12, 18, and 41 hours after closest approach to Uranus, a sequence of wide- and narrow-angle images of the planet's illuminated crescent were obtained at phase angles of approximately 157°, 153°, and 147°. The wide-angle images encompassed all or almost all of the illuminated disk, whereas the narrow-angle images were centered close to the nominal limb of the planet, near the center of the crescent, to capture the brightness variation above the nominal limb. Because of the geometry of the encounter and the high obliquity of the planet's axis of rotation with respect to the normal to the ecliptic, the illuminated portion of the planet was limited to low latitudes. In the analyses discussed in this paper we restrict ourselves to data obtained at a latitude of approximately 19.5°.

Table 1 summarizes several pertinent characteristics of the images analyzed here. These include the image identification number (flight data system, or FDS, count), the camera, filter, exposure time, effective wavelength of the camera/filter combination for a source having the Sun's spectrum, phase angle, and linear resolution in the absence of smear. Image smearing arose from a combination of the spacecraft's motion and small drifts in the camera's pointing direction during the time of an exposure (limit cycle motion). For the images obtained at 12, 18, and 41 hours after closest approach, the smear due to the spacecraft's motion was about 2.8, 1.9, and 0.8 km/s, respectively, while the limit cycle motion was approximately 0.6 pixels/s for the narrow-angle camera and 0.1 pixels/s for the wide-angle camera. Thus all of the wide-angle images were smeared

TABLE 1. Voyager Image Characteristics

FDS	Filter	Phase Angle, deg	Linear Resolution, km/lp	Exposure Time, s	Effective Wavelength, μm
26862.12	WA-green	157.5	78	0.48	0.56
26862.24	WA-blue	157.4	78	0.36	0.47
26862.36	WA-orange	157.1	80	1.92	0.60
26863.00	WA-violet	156.8	82	0.96	0.43
26863.12	NA-clear	156.8	11.0	0.72	0.47
26863.24	NA-green	156.7	11.2	2.88	0.56
26870.17	WA-green	152.9	118	0.72	0.56
26870.23	WA-orange	152.9	118	2.88	0.60
26870.35	WA-blue	152.8	120	0.48	0.47
26870.41	WA-violet	152.8	120	0.96	0.43
26870.47	NA-clear	152.8	16.2	0.96	0.47
26870.53	NA-green	152.8	16.2	5.76	0.56
26901.58	WA-green	147.4	278	0.96	0.56
26902.10	WA-orange	147.4	280	3.84	0.60
26902.22	WA-blue	147.5	280	0.48	0.47
26902.28	WA-violet	147.5	280	1.44	0.43
26902.34	NA-clear	148.0	38	1.44	0.47
26902.46	NA-green	148.0	38	5.76	0.56

by less than a pixel, the clear filter images of the narrow angle camera were smeared by about a pixel, and the green filter images of the narrow angle camera were smeared by several pixels. The effective resolution of the images taken with the narrow-angle camera is therefore close to the intrinsic resolution of slightly better than 2 pixels or 1 line pair and so is substantially less than the atmospheric scale height of the lower stratosphere (about 30 km) for the 157° and 153° narrow-angle images and comparable to it for the 147° ones.

The raw images of Table 1 were subjected to a series of photometric and geometric corrections to create data of a quality suitable for analyses. Initial processing of the pictures was conducted at the Jet Propulsion Laboratory's (JPL) Multi-mission Image Processing Laboratory (MIPL) facility, where standard algorithms, based chiefly on extensive prelaunch calibrations of the camera, were applied. The photometric and geometric corrections were made on a pixel by pixel basis and included removal of dark current (based on images taken close to the Uranus encounter), shading corrections to allow for the nonuniform response across the vidicons, corrections for nonlinear response, conversion to absolute reflectivity units (I/F) based on ground calibration data and supplemented by in-flight test results [*Danielson et al.*, 1981], corrections for geometrical distortions, and removal of obvious noise spikes and the camera's reseau marks. MIPL also supplied an ephemeris for the encounter (spacecraft event data record (SEDR)) that provides a postfacto determination of the spacecraft's three-dimensional position relative to the planet and the nominal pointing direction of the camera.

Further processing of the received images and ephemeris was carried out at the image-processing facilities of the Space Science Division at NASA Ames. Additional photometric processing included applying corrections for the absolute calibration of the images and removing background light due chiefly to sunlight scattered into the vidicon at the high phase angles of observation. To check on and to improve the absolute calibration of the images for each camera/filter combination of interest, we obtained disk-integrated brightnesses of images taken at several low phase angles, fitted these brightnesses to a quadratic function of phase angle, extrapolated these results to 0° phase angle, and compared the extrapolated values with ones derived by integrating the geometric albedo spectrum of

Uranus obtained by *Neff et al.* [1984] over the spectral response function of the camera/filter combination [*Danielson et al.*, 1981]. This methodology and its results are described in much more detail by T. V. Johnson et al. (manuscript in preparation, 1987]. These corrections ranged from almost nothing to about 10% for the camera/filter combinations of Table 1. We suspect that the absolute calibration is now good to about 5% and the relative I/F values of this paper, i.e., for a given camera/filter, are good to about 1% in the brighter portions of the image.

The MIPL-supplied images display low but nonzero brightness at locations far removed from the planet and locations well within the unilluminated portion of the planet. We removed this residual background brightness in two steps. First, we fitted points in the above locations to a two-dimensional quadratic function of location in the image (line and sample number) and subtracted this function from the brightness at every pixel. The points used for determining the quadratic function were obtained by averaging brightness values in boxes that were 5 × 5 pixels across at every 100 pixels in line and sample number that fulfilled the condition of either being sufficiently far from the planet or sufficiently far into the unilluminated portion of the planet. The fitted points typically had an rms residual of 0.001 in I/F units with respect to the derived function ($I/F = 1$ for a perfectly reflecting lambert surface illuminated at normal incidence). A final correction for background light was applied to individual line scans by fitting a one-dimensional quadratic function to points well off the planet and well inside the terminator.

Although the SEDR files provide extremely accurate positions for the spacecraft relative to the planet, the camera-pointing information needed to be corrected because of a lack of knowledge of where the scan platform was in its limit cycle motion. We derived these pointing corrections by comparing the observed and predicted locations of the limb on the image. Using a nonlinear least squares iterative program, we derived two correction factors for the narrow-angle images and three for the wide-angle images. The two parameters common to both cameras were orthogonal pointing corrections, ds and dl, that are the sample and line number displacements, in units of pixels, between the "actual" location of a given latitude/longitude point on the planet and the location predicted from the SEDR files. The limb was operationally defined in this analysis by the location of points having half the intensity of nearby peak intensity points. In general, dl and ds were at most 10 pixels for the wide-angle images. One of the narrow-angle images required a pointing correction of about 150 pixels. Since the wide-angle images contained 90° of limb arc or more, it was practical to derive the radius of the half-intensity level as an additional free parameter from the limb fits. In this and all subsequent analysis described below, the equipotential surface of Uranus was approximated as an ellipsoid having a polar flattening of 0.024 [*Elliot et al.*, 1981]. The narrow-angle images did not show enough limb arc to properly determine the radius, so the equatorial radius was set equal to 25,600 km, a typical value found from the wide-angle images.

The final step in the data reduction was to obtain line scans in selected locations. In carrying out this step, it was useful to transform the geometry from a two-dimensional Cartesian system to a polar coordinate system having its origin at the projected center of the planet's image. Scans were taken in the radial direction from well off the planet's limb to well inside it. I/F values were obtained at a radial increment of about one

pixel by averaging about 10 pixels in the cross-track direction. To further improve on the photometric accuracy of this data, we averaged together five adjacent scans.

For each such sample location, we used the corrected SEDR to derive the latitude, longitude, phase angle, solar illumination angle, camera viewing angle, and altitude with respect to a reference radius from the planetary center for each point along the line of sight. In practice, the solar illumination angle and the phase angle varied very little along the line of sight and could be considered to be constant. However, the other geometrical parameters varied significantly, even for points somewhat interior to the nominal limb. A further description of the manner in which this information was used in our analyses is contained in the next subsection.

2.2. Radiative Transfer

Two sets of radiative transfer programs were used to analyze the high phase angle images. A multiple-scattering code for a plane parallel geometry was used to simulate data obtained with the wide-angle images at positions somewhat interior to the limb. These simulations were directed at deriving information on the presence of stratospheric haze and on the average size and number density of the haze particles at a level close to slant path optical depth unity. An inversion program for an ellipsoidal geometry was applied to the narrow-angle images to derive vertical profiles of the total extinction coefficient (aerosol plus gas). These results were further processed to remove the contribution of molecular extinction and thus isolate the contribution of aerosols to the observed limb profile. Aspects of these computer programs and our data analysis approach are described below and in Appendices A and B.

The multiple-scattering code for plane parallel geometry is based on a scalar adding/doubling approach to solving the multiple-scattering problem [Rages and Pollack, 1983]. Allowance is made for variations in the scattering properties of the atmosphere with altitude by dividing the atmosphere into a sequence of homogeneous layers. The scattering calculations include Rayleigh and Raman scattering by gas molecules, absorption by gaseous methane, scattering and absorption by haze particles, and scattering and absorption by methane cloud particles [Pollack et al., 1986a, b]. All calculations were done at a sequence of monochromatic visible wavelengths, and the results were then convolved over the camera/spectral response function to yield I/F values for comparison with the observed values.

As indicated above, a scalar adding/doubling program was used to compute the predicted intensities. Since molecular Rayleigh scattering makes an important contribution to these intensities for typical haze models of this paper, we needed to compare the intensities obtained with a scalar program with those found with a matrix adding/doubling code that included polarization effects. For typical geometries simulated in this paper we found that the matrix intensities were approximately 3% larger than the scalar values. Furthermore, this percentage difference was almost the same for all the phase angles of interest. Thus the effect of not performing matrix calculations is comparable to that of a 3% error in the absolute calibration of the filters. Such an error will not significantly affect the model parameters derived in this paper, nor will it alter any of our conclusions.

The baseline model atmosphere of Uranus used in these simulations is as follows. The molecular atmosphere contained, by number, 15% He, CH_4 that was at most 2.3%, and H_2 that made up the remainder [Hanel et al., 1986; Tyler et al., 1986]. The mole fraction of methane was assumed to be equal to 2.3% at pressures in excess of 1.3 bars, to follow the nominal, relative humidity profile of Lindal et al. [this issue] in the upper troposphere, and to have a constant value in the stratosphere equal to its value at the tropopause. We used a temperature profile derived from pertinent Voyager data [Lindal et al., this issue].

The haze aerosol was assumed to be present from the top of the methane clouds at a pressure level of 900 mbar [Tyler et al., 1986] to a low pressure level in the stratosphere, whose exact value is not important for this analysis. Initially, we assumed that the haze had altitude-independent properties and was uniformly mixed with the gas. We fitted the data to estimate the mean size, mixing ratio, and imaginary index of refraction of the haze particles. The latter was modeled by a power law dependence on wavelength [Pollack et al., 1986a] and, thus, can be characterized by two free parameters: its value at a reference wavelength (0.55 μm) and the power law index. In subsequent iterations, we used a vertical profile based on the microphysical model described below to allow approximately for the altitude dependence of the size distribution and number density of the haze. This model was constrained to match approximately the radiative transfer results from the first iteration. During the next iteration, we again solved for four free parameters: the two imaginary index parameters and particle size and number density scaling factors, SR and SN. The modal sizes of the microphysical model were uniformly multiplied by SR, and, in a similar vein, the number densities of aerosols were uniformly multiplied by SN. Thus we assumed that the vertical profile of the aerosol model is approximately correct and that it only needed to be multiplied by two scaling factors to bring it into agreement with the observations. If the scaling factors are not too large, as was true on even the second iteration, this assumption is a reasonable one. For the first iteration, the real index of the aerosols was set equal to 1.5, a typical value for aerosols [Rages et al., 1983], while in subsequent iterations it was set equal to values appropriate to the hydrocarbon hazes of interest: 1.44 for ethane, 1.33 for acetylene, and 1.42 for diacetylene.

In carrying out the above multiple-scattering simulations we used Mie theory to specify the single-scattering characteristics of the haze particles. For this purpose the size distribution of the haze particles was expressed in terms of equal-volume spheres. The use of Mie theory and the use of equal-volume spheres are appropriate approximations for the non-spherical ice particles of interest, since the results of our calculations yield modal particle radii that are less than the wavelength at all levels contributing significantly to the observed radiance [Pollack and Cuzzi, 1980]. Also, the high phase angles and hence the small scattering angles of the geometries of interest imply that Mie theory should be an excellent approximation [Pollack and Cuzzi, 1980].

The methane cloud in the baseline model was characterized by a Jupiter-type phase function ($g_1 = 0.8$, $g_2 = -0.75$, $h = 0.95$) [Smith and Tomasko, 1984], a wavelength-independent optical depth of 0.45, an extinction profile proportional to the square of the gas density, and a small amount of absorption, assumed to be due to embedded haze particles. These parameters were largely derived from initial fits to low phase angle, spatially resolved Voyager images of Uranus [Pollack et al., 1986b; K. Rages et al., manuscript in preparation, 1987). These results, including refinements to the above parameters, will be given in a separate paper (K. Rages et al., manuscript in preparation, 1987). In a later section of this

paper we will examine the sensitivity of our results to the above choices of methane cloud properties and the mixing ratio profile for gaseous methane.

Simply for the purpose of defining the effective latitude and emission angle of data points from the wide-angle images, we fitted one-dimensional scans of the images to the predictions from a simple model of vertical structure. The model used was an exponential atmosphere containing three free parameters: an albedo-weighted single-scattering phase function at the mean phase angle, the extinction coefficient at a reference altitude, and the scale height of the extinction coefficient. An ellipsoidal geometry program of the type used to invert the narrow-angle images, which is described below, was used to simulate the scan, derive the values of the fitting parameters, and to define a brightness-weighted average value of latitude and emission angle for points of interest along the scan. This procedure was carried out for each of the wide-angle images used in our analysis.

Once this had been done, points at a common latitude were selected for comparison with the results of the adding/doubling program. For the purposes of this paper, we used points at a latitude of 19.5° so that these results could directly be incorporated into the analyses of low phase angle images. Points somewhat interior to the limb were selected to insure the validity of the plane parallel approximation.

An inversion algorithm similar to that described by *Rages and Pollack* [1983] and applied to Titan's limb, was used to derive vertical profiles of the total-aerosol plus gas-extinction coefficient from analysis of the narrow-angle images. Basically, this algorithm takes advantage of the dominant role played by single scattering in determining the observed I/F for the oblique viewing geometry characterizing altitudes for which the slant path optical depth is less than unity. Modifications to the inversion protocol of *Rages and Pollack* [1983] included employing ellipsoidal shells rather than spherical shells to describe equipotential surfaces (the extinction coefficient was assumed to be constant on these surfaces), obtaining the mean value of the emission angle to use in the multiple-scattering term characterizing large slant path optical depths from a procedure similar to that of *Wallach and Hapke* [1985], extending the retrieval to somewhat greater depths, treating the albedo-weighted single-scattering phase function as an additional free parameter to be fitted to a given scan, and including planet reflected light in the source term for scattering at low slant path optical depths. The last improvement is described briefly below and in detail in Appendix A.

We modeled the observed radiances by considering two asymptotic solutions to the radiative transfer problem and joining them in a smooth fashion near slant path optical depth unity. At locations well above the limb, we approximated the scattering problem by considering singly-scattered sunlight and planet-reflected light, with full allowance for the spherical geometry. At locations well inside the limb, we approximated the problem as a multiple-scattering situation with a plane parallel geometry. The formulation of *Rages and Pollack* [1983] neglected planet-reflected light in the source function for light scattered at high altitudes. This was a reasonable approximation for a low-albedo object, such as Titan. However, its neglect is less justifiable for Uranus, since the planet has a high albedo and since the combined aerosol/gas scattering phase function is not very large at the phase angles of interest. In Appendix A we present a detailed description of the protocol used for this paper that permits planet-reflected light to be incorporated into the source function for light

scattered at high altitudes. In a typical case we found that this component of the source function contributed about 25% of the light scattered to the camera at a phase angle of 157° and about 30% of the total at a phase angle of 148°.

The end product of the inversion algorithm is a determination of the total extinction coefficient (gas plus aerosol) as a function of altitude. The extinction coefficient is derived by assuming that the product of the single-scattering albedo and phase function at the observed phase angle is independent of altitude. This product is determined by matching the line scan near slant path optical depth unity, where the extinction coefficient and the above product are separable.

To convert these results into a somewhat more useful form, we needed to relate the altitude scale to a pressure scale and to determine the contribution to the extinction coefficient made by molecular scattering alone. A profile of the total extinction as a function of pressure can be determined for a given microphysical model by summing the aerosol extinction, as obtained by applying Mie Theory to this model, and gas extinction, as obtained from the standard relationship between Rayleigh extinction and pressure [*Hansen and Travis*, 1974]. The total extinction derived in this way is set equal to the total extinction derived from the limb scan inversion at an altitude near slant path optical depth unity, thereby defining the pressure at this altitude. Finally, using the equation of hydrostatic equilibrium and the Voyager temperature profile [*Lindal et al.*, this issue], we readily determined the pressure and molecular scattering coefficient at all other altitudes.

For the purpose of comparing an observed vertical profile with the predictions of a given microphysical model, it is useful to isolate the aerosol component of the inversion profile. In Appendix B we present a derivation of this isolation for the higher-altitude portion of the atmosphere, where the slant path optical depth is less than unity. An aerosol term, which we call "haze scattering parameter," can be obtained by subtracting a quantity involving Rayleigh scattering factors from a quantity involving the total extinction coefficient and other factors determined by the inversion protocol. The haze scattering parameter is the product of four aerosol parameters: the aerosol single-scattering albedo, extinction coefficient, phase function at the observed phase angle (or equivalently observed scattering angle), and a factor that involves an angular integration of the phase function. This last factor provides a measure of the enhancement of the aerosol component of the light scattered to the camera owing to planet-reflected light. For a given microphysical model, this haze scattering parameter can readily be calculated. The adequacy of a given microphysical model can be assessed, in part, by comparing its predicted altitude profile for the haze scattering parameter with the profile derived from the inversion algorithm.

2.3. Photochemical Model

Simulations of the photochemistry of methane in Uranus' stratosphere were carried out to determine the vertical profiles of hydrocarbons that could condense in the lower stratosphere. From this modeling it was possible to determine the major species expected to form condensate hazes, the pressure levels at the top of the condensation regions, and the net downward fluxes of condensate gas species into the regions of condensation. This modeling is described below.

Solar UV radiation, chiefly Lyman alpha, dissociates gaseous methane into a number of free radicals in the upper stratosphere. Optical depth unity for Lyman alpha occurs at an altitude of approximately 220 km above the tropopause,
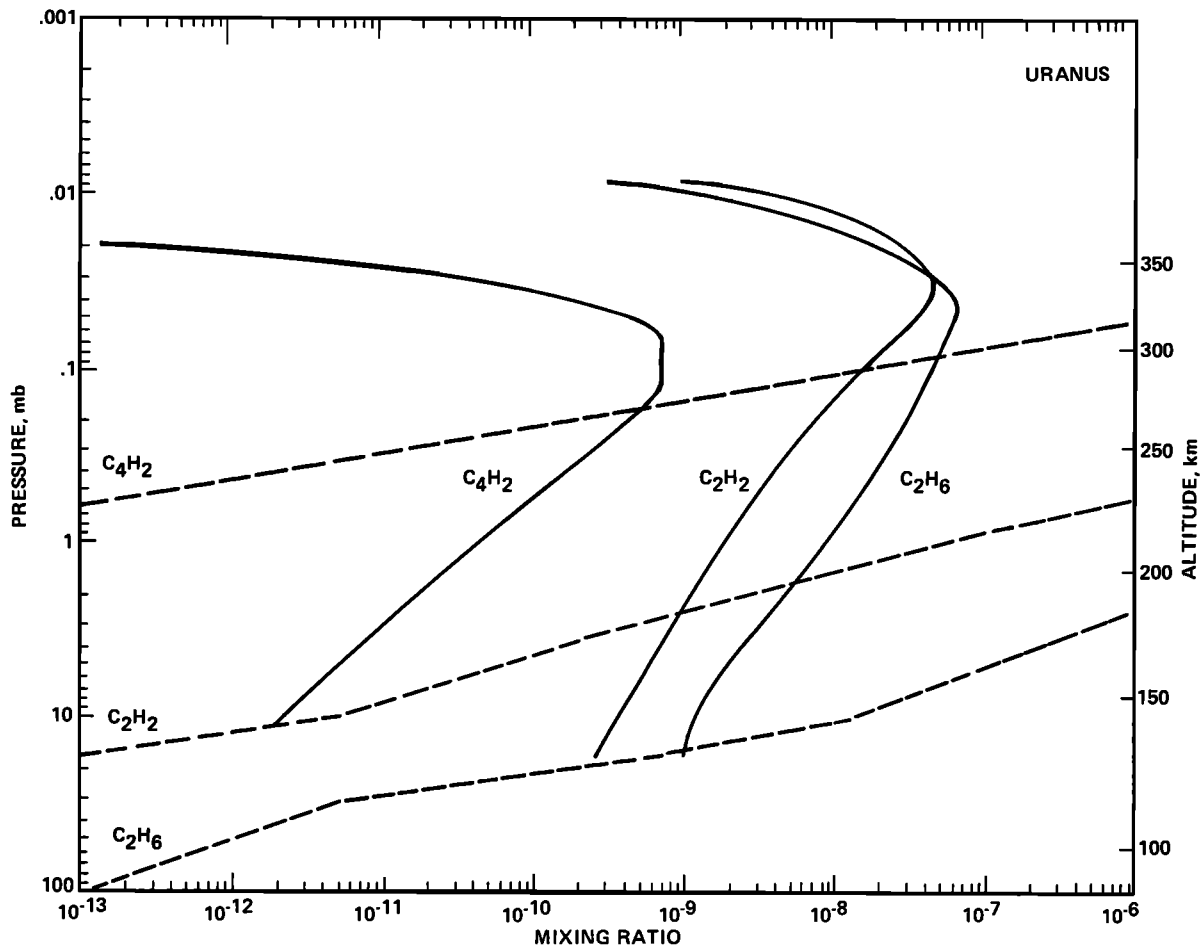
Fig. 1. Molar mixing ratio of lower order hydrocarbons as a function of altitude above the base of the troposphere. The solid lines show results from the photochemical model in the absence of condensation, and the dashed lines show the values at the saturation vapor pressure in equilibrium with condensed ice. Where the two lines intersect for a given hydrocarbon, its condensation begins.

where the pressure is approximately 0.1 mbar. A series of photochemical reactions among the free radicals, methane, and molecular hydrogen leads to the production of stable lower-order hydrocarbons. The kinetic pathways and reaction rates were based on the methane photochemisty of Atreya [1984]. Very useful constraints on the photochemistry of methane in Uranus' stratosphere are provided by analyses of the Voyager ultraviolet spectrometer (UVS) observations [Atreya et al., 1986; Herbert et al., this issue]. The Voyager UVS solar occultation light curves can be reproduced successfully by the methane photochemical model having an eddy diffusion coefficient of 10^4 cm^2/s at the methane homopause. This homopause is located approximately 300 km above the tropopause, where the pressure is 0.02 mbar. In accord with this analysis and those for the atmospheres of Jupiter and Saturn, we assumed that the eddy diffusion coefficient scaled inversely as the square root of the total gas density [Atreya et al., 1981; Atreya, 1982].

Aerosols are produced by the photochemistry of methane in the stratosphere of Uranus when lower-order hydrocarbons condense to form their respective ices. Ethane and acetylene represent the two chief condensate species. As illustrated in Figure 1, these species are produced in the gas phase by methane photolysis occurring in the upper stratosphere. They are then transported down to the lower stratosphere, where condensation to their solid phases takes place at the low ambient

temperatures. Using the temperature profile retrieved from the Voyager radio occultation [Lindal et al., this issue] and expressions for the saturation vapor pressure of hydrocarbons obtained from laboratory data [Stull, 1947; Ziegler, 1959; Ziegler et al., 1964], we have estimated the pressure levels at which condensation is expected to begin or, more precisely, the levels at which 100% relative humidity is reached. We find that condensation of ethane and acetylene commence at pressure levels of approximately 14 and 2.5 mbar, respectively.

In addition to these two condensates the photolysis of acetylene in the vapor phase results in the production of diacetylene, C_4H_2, which can condense at somewhat higher altitudes than acetylene. Diacetylene is the first higher-order polyacetylene ($C_{2n}H_2$, $n = 2, 3, 4$, etc.) formed from methane photolysis. We have updated the photochemical scheme of Yung et al. [1984] to make use of the recent laboratory measurements of Glicker and Okabe [1987] of the absorption cross sections and quantum yields of diacetylene photolysis in our analysis of polyacetylene production on Uranus. Figure 2 shows the photochemical pathways by which diacetylene is produced. Figure 1 illustrates the calculated vertical profile of C_4H_2 and the location of its condensation level. This condensation level is located at a pressure level of about 0.1 mbar.

The condensation levels for ethane, acetylene, and diacetylene are summarized in Table 2. Uncertainties in these values arise from uncertainties in the temperature profile and the
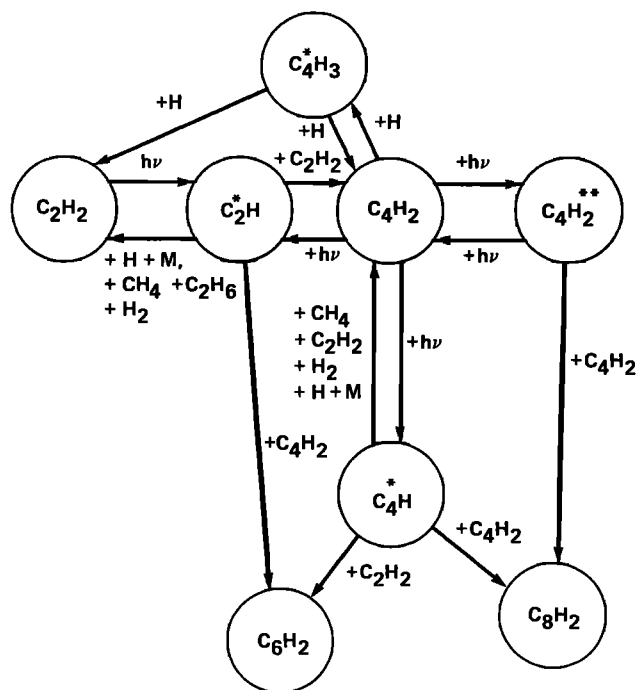
Fig. 2. Photochemical pathways for producing diacetylene from the photolysis products of methane. An asterisk means the radical is assumed to be in photochemical equilibrium, while a double asterisk means an excited molecule.

vapor pressures. We have evaluated the uncertainty in the temperature profile on the basis of the variance exhibited by the Voyager radio occultation ingress and egress profiles, the stated retrieval errors for each of these profiles, and the stated uncertainty in the Voyager UVS temperature at the μbar level [Lindal et al., this issue; Herbert et al., this issue]. The vapor pressure of ethane near its condensation temperature is believed to have an uncertainty of only about ±10%, while the vapor pressures of acetylene and diacetylene have uncertainties of factors of an order of magnitude or larger, on the basis of the need to extrapolate their measured vapor pressures to lower temperatures.

On the basis of these considerations, we estimate that the condensation levels for ethane, acetylene, and diacetylene lie between 7 and 20 mbar, 0.6 and 5 mbar, and 0.02 and 0.5 mbar, respectively. We note that the extrapolation of the vapor pressure data for acetylene and diacetylene is likely to lead to an overestimate of their actual vapor pressures at low temperatures. Hence the true condensation level of acetylene is likely to lie at a lower pressure than the value given in Table 2. The actual condensation level of diacetylene might lie at

either a higher or a lower pressure than the value given in Table 2 in view of large uncertainties associated with both its vapor pressure and the temperature profile at pressures less than 0.1 mbar.

The condensation of diacetylene limits the production of higher-order polyacetylenes [Romani and Atreya, 1986], with the production rate being half of what it would be if no condensation occurred. Because of this limitation and the already low UV optical depth of diacetylene due to its low mixing ratio, we have not modeled the production and condensation of higher-order polyacetylenes.

The photochemical model also permits us to determine the rate at which ice condensation is occurring. This photochemical ice production rate is obtained by determining the net downward flux of a given gas species at altitudes just above their condensation level. Since all of the hydrocarbons condense well below the homopause, this flux, F, could be calculated directly from the photochemical model using the standard equation:

$$F = -KN_g df/dz \qquad (1)$$

In equation (1), K is the eddy mixing coefficient, N_g is the total atmospheric gas number density, f is the mixing ratio of the condensing species in the gas phase, and z is the altitude. In evaluating fluxes and hence ice production rates from this equation we included the vapor pressure constraint in the photochemical calculations. Thus whenever the value of f calculated from the photochemistry implied a relative humidity greater than 100%, we reset its value to that given by the saturation vapor pressure.

Table 2 summarizes the values of the photochemical ice production rates found for ethane, acetylene, and diacetylene, as well as the pressures at the top of the condensation regions and other relevant properties of these ices. According to these calculations, the mass production rates of ethane, acetylene, and diacetylene represent approximately 80, 17, and 3% of the total ice production rate. The above rates pertain to the latitude of Uranus that we are analyzing in this paper. For the orientation of Uranus' axis of rotation relative to the Sun at the time of the Voyager flyby, the ice production rates increase only by a factor of 2 from equator to sunlit pole owing to the change in the diurnally averaged solar illumination.

We estimate that the absolute values of the ice production rates of Table 2 have uncertainties of about a factor of 2 owing to uncertainties in some of the photochemical reaction rates and the values of the eddy diffusion coefficient. The corresponding uncertainty in the ratio of these rates for the different condensate species is also a factor of 2. We base these estimates of uncertainty upon previous modeling of methane photochemistry for Jupiter and Saturn [Atreya and Romani, 1985]. The uncertainty in the condensation levels of the hy-

TABLE 2. Properties of Hydrocarbon Ices

Species	Formula	Density,[a] g/cm^3	Refractive Index[b]	Mass Flux,[c] g/cm^2/s	Condensation Top, mbar	Level Bottom, mbar
Ethane	C_2H_6	0.69	1.44	2×10^{-17}	14	22
Acetylene	C_2H_2	0.73	1.33	4×10^{-18}	2.5	3.5
Diacetylene	C_4H_2	0.74[d]	1.42[d]	1×10^{-18}	0.1	0.15

[a]Obtained from Donnay [1972] and Chemical Rubber Company [1975].
[b]Obtained from Vogel [1948] and Chemical Rubber Company [1975].
[c]Derived from the photochemical model.
[d]Value for the liquid phase.

drocarbons, especially those for acetylene and diacetylene, adds a further element of uncertainty to the ice production rates of Table 2. Decreasing the pressure level at which acetylene condenses from 2.5 mbar, the nominal value of Table 2, to 0.6 mbar, an extreme but possible lower bound, results in an increase in the acetylene ice production rate of a factor of 1.6. Finally, as discussed in a later section, allowing for the photochemical production and localized condensation of diacetylene within its condensation region could lead to a large increase in its ice production rate in comparison to the value given in Table 2.

2.4. Microphysical Model

A microphysical model of aerosol formation and evolution has been constructed and applied to the Uranian stratosphere to evaluate the altitude profile of the particles' size distribution and number density. Through comparisons of these predictions with the Voyager observations, we have been able to constrain two of the free parameters of the model: the total mass production rate of aerosols and the amount of electrical charge on the particles. The remaining free parameters were derived from the results of the photochemical model. They include the locations of the aerosol production regions, relative production rates for the three condensing species, the bulk aerosol density, refractive index, and eddy mixing coefficients (cf. Table 2 and previous subsection). However, we explored the sensitivity of our results to large changes in some of these parameters, such as the relative production rates and the location of the condensation levels. We also examined the impact of particle shape and refractive index on our results. Below, we describe briefly the physics and numerics of this microphysical model.

Following *Toon et al.* [1980], a one-dimensional model of the atmosphere was divided into discrete altitude bins. Aerosols at each altitude level were distributed among size bins. The number of particles in each size and altitude bin was allowed to change owing to various physical processes such as condensation, sedimentation, coagulation, and eddy diffusion. Thus particles form by vapor condensation, grow by coagulation and vapor deposition, and move vertically owing to gravity and turbulent motions. Starting with an atmosphere free of aerosols, the model was stepped through time. At each time increment the rate of change in the number of particles in each bin was calculated. This rate was multiplied by the time step to get a net change in particle number. When the number in each bin reached a constant value, the steady state aerosol distribution as a function of altitude and particle size was the result.

Forty-six altitude/pressure bins spanned the pressure range of interest, 0.01 mbar to over 2 bars. An altitude of 0 km was assigned to 3 bars, and altitudes throughout the rest of the atmosphere were calculated by application of hydrostatic equilibrium and the ideal gas law. The temperature-pressure profile was derived from the Voyager radio occultation experiment [*Lindal et al.*, this issue]. The size of the bins was chosen so that two or more bins spanned one pressure scale height.

The size bins were such that each successive bin represented a doubling in volume. The smallest-size bin corresponded to a particle radius of 0.01 μm. If a single molecule of aerosol material has dimensions of the order of angstroms, the smallest bin therefore contained particles which were conglomerations of tens of molecules.

As mentioned above, each model was started at time $t = 0$ with no aerosols in the atmosphere. Initially a time step of typically 10^4 s was used as mass was injected into the upper altitude bins and the smallest-volume bins. High coagulation rates here prevented the use of a larger time step. As these upper bins approached steady state, however, they became less sensitive to the size of the time step as the sum of the rates affecting them approached nearly zero. Lower altitude layers had in general slower coagulation rates and so needed a larger time step to achieve steady state. These requirements led to the use of an exponentially increasing time step. Over the model run, the time step slowly increased to a maximum value of 100 to 1000 times the initial value. Typical models ran for 4000 time steps and constituted a total (model) time of 1 to 2×10^{10} s.

The code describing each of the processes outlined below was tested by "turning off" all other processes and letting the one remaining operate on an initial population of particles. The results of these experiments were compared with known analytic solutions. For example, a distribution of particles at a fixed altitude was subjected to coagulation alone over many time steps. As expected, the mean size of the particles increased with time, while the shape of the distribution was preserved. To test the eddy diffusion algorithm, particles were distributed in altitude with a gradient opposite of that of the gas density. After being subjected to many time steps (without sedimentation, coagulation, etc., operating on them), the particles became evenly distributed with the gas.

For each process as well as the full-up model run, mass conservation was maintained. The mass loss from the atmosphere is simply the mass of the particles falling out the bottom of the lowest altitude layer. When this converged to a constant value (equal to the mass input), the model had reached steady state.

On the basis of the results of the photochemical model, there were three regions of the model atmosphere in which aerosol mass was continually being produced. These three production regions correspond to levels at which the preponderant condensation of diacetylene, acetylene, and ethane, respectively, was occurring. The top of a given production region was defined by the level at which a given hydrocarbon first condensed. Comparison of the saturation vapor pressure curves with extrapolated partial pressures from the regions just above the condensation points implied that almost all condensation could be expected to occur within one third to half a scale height of the top of the condensation levels. The pressure boundaries that define the regions of ice condensation in our calculations are shown in Table 2. For simplicity, the production rates in the production regions were characterized by a triangular profile that peaked at the center of the region and became zero at its two boundaries. The results of our simulations are not sensitive to these simplifications. The total production rate of aerosols, i.e., the sum of the production rates in the three regions, was a free parameter of these calculations, while the relative production rates of our base models were constrained to agree with those given by the photochemical model and summarized in Table 2. We also investigated the effects of alternative choices.

In the production region corresponding to the places where diacetylene was condensing, mass was added at a given rate to the smallest-volume bin. This assumption implies that the resulting particle size distributions within the diacetylene condensation region are not expected to be entirely accurate. Physically, this treatment of the condensation of diacetylene corresponds to homogeneous nucleation of a supersaturated vapor, which occurs in very clean environments, i.e., ones lacking condensation nuclei. Accordingly, the pressure where con-

densation commences may be slightly higher than the value we have chosen based on 100% relative humidity, since homogeneous nucleation usually requires a high degree of supersaturation (cf. Figure 1).

The presence of sedimentating diacetylene particles at the levels where acetylene condensation is taking place and the presence of diacetylene/acetylene particles at the levels where ethane condensation is occurring implies that heterogeneous nucleation commencing at relative humidities just slightly in excess of 100% can be expected. Therefore condensation at these levels was assumed to take place on already existing particles and so did not generate new particles. The mass production due to condensation in the two lower-altitude regions was parameterized so that a given amount of mass per unit time was deposited into an altitude layer. The mass was distributed among the volume bins at that altitude proportional to the surface area of the particles, $N_p(r)r^2$, where $N_p(r)$ is the differential number density of particles of radius r. Alternatively, the mass was distributed proportional to $N_p(r)r$ to account for the effect of the curvature of the surface of the particles on the equilibrium vapor pressure [Fleagle and Businger, 1963]. In all the calculations discussed in this paper, we used the latter prescription for distributing condensed vapor. The mass input into the layer was assumed to be constant throughout time. The resulting increase in particle size due to condensation from the vapor was approximated by moving some fraction of the particles in each size bin to the next larger bin. The net exchange rates were calculated from mass and particle number conservation considerations for this process.

The sedimentation rate was determined from the aerosol fall velocity w; particles falling both into and out of the altitude bin were considered. The fall velocity was calculated from formulae given by Kasten [1968]. They are valid for a Knudsen number (Kn, the ratio of the gas mean free path to the radius of the falling particle) either less than or greater than unity. In the region of the Uranian atmosphere considered for these models, the Knudsen number was always greater than 1.

The coagulation rate for particles in a size bin J depends on the number of particles in bin J, the number in every other bin J', and the coagulation kernel between the two particle sizes J and J'. For the kernel we used a formula from Fuchs [1964], which again is valid for both large and small Kn values. The expression for the kernel contains a sticking coefficient which, in the absence of charging, is taken as unity. When the aerosols have a charge of Q per unit radius, the sticking coefficient s between a particle of radius r_1 and one of radius r_2 is given by

$$s = \exp\left[(-Q^2 r_1 r_2)/(kT[r_1 + r_2])\right] \qquad (2)$$

where k is Boltzmann's constant and T is the temperature.

Both the sedimentation and coagulation rates can be modified, in a limited way, to describe nonspherical particles. As described by Toon et al. [1980], a shape factor X_k modifies the coagulation kernel, and the corresponding factor X_s modifies the sedimentation velocity.

Rates of vertical motion due to eddy diffusion were calculated by comparing the eddy diffusion flux into an altitude layer with the flux out of the layer. In all but one run we used the profile for the eddy diffusion coefficient derived from the Voyager UVS experiment and described in a previous section of this paper [Herbert et al., this issue]. The net effect of eddy diffusion on the Uranian aerosol models was very small in these cases, since the sedimentation velocity of an averaged sized particle greatly exceeded an equivalent velocity due to

eddy mixing. However, we examined the effects on our results of a greatly increased eddy diffusion coefficient in the region spanning the three condensation zones that, hypothetically, could be engendered by the radiative effects of the ice particles.

Figure 3 illustrates the size distribution for microphysical model US5 that served as a base case for the fits to the Voyager data described in the next section. This model is characterized by a total mass production rate of 1.1×10^{-16} g/cm^2/s, the relative mass production rates of Table 2, no particle charging, a particle specific density of 0.7 g/cm^3, and particles having a spherical shape. The histograms in Figure 3 show the relative number of particles in the size bins of the microphysical model at three pressure levels.

We found it convenient and appropriate to fit the detailed size distributions to a log normal distribution, given by

$$n(r) = \frac{N \exp\left[-0.5(\ln (r) - \ln (r_m))^2/(\ln (\sigma))^2\right]}{rA} \qquad (3)$$

where n is the differential number density of particles of radius r, N is the total number density, r_m is the modal radius, σ is a measure of the width of the distribution, and A is a normalization constant equal to

$$A = \sqrt{2\pi} \ln (\sigma) \qquad (4)$$

The curves in Figure 3 illustrate the ability of this functional form to provide a good fit to the size distributions calculated with the microphysical model. Extinction cross sections calculated with the log normal distribution agree with those derived from the actual distribution to within about 5% at pressures of several tens of millibars and to 10–20% at pressures of a few millibars.

Owing to coagulation and vapor deposition, r_m monotonically increases with increasing pressure (cf. Figure 3). The size distribution has a very narrow width in the diacetylene condensation region (0.17 mbar) but attains a fairly constant and larger width at higher pressures.

The aerosol profiles calculated with the microphysical model are not very dependent on whether growth by condensation was assumed to be proportional to the particle
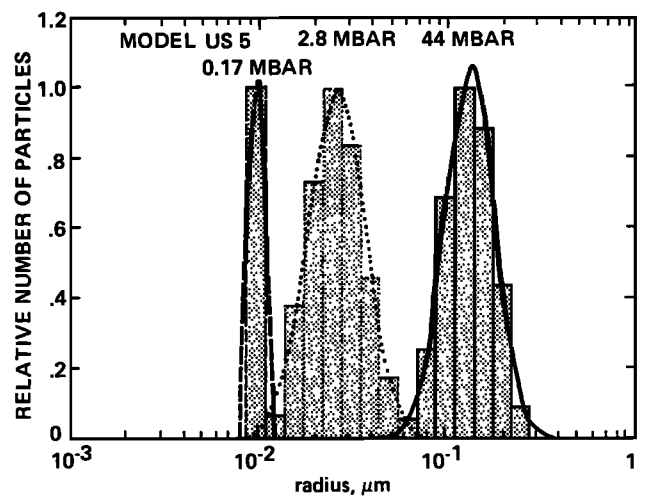

Fig. 3. Size distribution predicted by microphysical model US 5 (see text for details) at several pressure levels in the lower stratosphere. The histograms show the size distribution obtained directly from this model, while the smoothed curves show the log normal size distributions fitted to these histograms.

radius or surface area. As indicated earlier, a growth rate proportional to particle radius was used in the calculations reported here.

3. RESULTS

In this section we present estimates of the microphysical and radiative properties of the Uranian stratospheric aerosols derived by simulating the Voyager high phase angle images of the planet. The simulations are performed with an adding/doubling multiple-scattering code in the case of the wide-angle images and a spherical-scattering model for the narrow-angle, limb images. Where appropriate, the microphysical model and photochemical model are used to provide additional constraints on model parameters.

3.1. Wide-Angle Images

We have obtained estimates of the modal radius, number density, imaginary index of refraction, particle charging, and total mass production rate of the stratospheric hazes by simulating wide-angle images taken at phase angles of 148°, 153°, and 157° through the violet, blue, green, and orange filters. Table 3 summarizes the observed intensities and geometry for points on these images that are located on the disk of the planet, somewhat interior to the position of maximum intensity. These locations were chosen to enhance the appropriateness of using a plane parallel multiple-scattering code, while at the same time retaining the dominance of the stratospheric aerosols in determining the observed radiances. They were also selected to lie at roughly the same latitude.

The sixth column from the left in Table 3 (Rayleigh) shows the predicted intensities for model atmospheres containing only molecular scatterers and absorbers. While such an atmosphere would be expected to brighten toward the higher phase angles, the magnitude of the predicted increase is substantially lower than the observed increase for the three shorter-wavelength filters. In addition, the predicted I/F values at the highest phase angle are significantly smaller than the observed values for all four filters. The magnitude of these discrepancies is much larger than permitted by plausible uncertainties in the relative and absolute calibration of these filters. Thus they provide prima facie evidence for the presence of stratospheric aerosols, since almost all the observed radiance originates from the lower stratosphere.

The shape of the aerosols' phase function at the high phase angles (low scattering angles) of interest is dominated by their diffraction lobe, whose width is determined by the ratio of the mean particle size to the wavelength [Rages et al., 1983]. Thus we can constrain the mean particle size near slant path optical depth unity by fitting the data of Table 3. We can also constrain the number density of aerosols at this location by fitting data taken at several effective wavelengths, since the molecular scattering coefficient varies as the inverse fourth power of the wavelength, whereas the scattering coefficient of the aerosols depends on the wavelength to a lower power. Finally, very approximate constraints on the imaginary index of refraction can be derived by matching the data, since refracted light can also contribute to the phase function when the aerosols are transparent and since the fraction of multiply-scattered light increases as the particles become more transparent: Multiply-scattered light diminishes the amplitude of the observed phase variation and increases the I/F value at a given phase angle.

As indicated in the previous section, the vertical profiles of aerosol properties predicted by the microphysical model are used in our radiative transfer simulations of the data in Table

3. Since these profiles are determined by few free parameters, we can constrain several of them by fitting the Voyager intensities and specify the remainder on the basis of the photochemical model. In particular, we determined size and number density scaling factors, SR and SN, by fitting the data. These scaling factors were in turn related to the total mass production rate dM and particle charging Q employed in the microphysical model. In general, increasing dM increased both the mean size and number density of the particles at a given pressure level, while increasing the charge per unit radius decreased the mean size and increased the number density. For scaling factors that lay close to unity, modest adjustments in dM and Q can result in an optimum fit to the data. We carried out several iterations between the radiative transfer simulations and the aerosol models so that the scale factors were close to unity on the last iteration.

Although it might seem that there are a sufficient number of constraints to specify a unique model and determine its two free parameters from the wide-angle images, we in fact have studied a broad suite of models for several reasons. First, the shape of the particles could affect the results by influencing the particles' fall velocities and hence the vertical profile of their mean size and number density, as predicted by the microphysical model. Second, there are significant uncertainties in the relative production rates of ices in the three condensation regions and in the locations of these regions. Thus the values of these parameters given by the photochemical model and summarized in Table 2 should be viewed simply as first approximations to the actual values. Third, there is a need to explore the sensitivity of our results to the values chosen for other model parameters, such as methane cloud properties, the mixing ratio profile for gaseous methane, and the eddy mixing profile, especially in the condensation regions.

Table 4 summarizes the characteristics of the models investigated in this paper. The particles of models whose number begins with UF have the shapes of thin disks with a thickness equal to 0.1 times the radius, whereas those of models beginning with US have equidimensional shapes. The other major distinction among the various models of Table 4 is the relative production rates in the three regions of ice condensation. Values for these rates range from 3, 17, and 80% for the diacetylene, acetylene, and ethane condensation regions, respectively, in accord with the best a priori photochemical model predictions, to 100, 0, and 0%. In the case of the UF 10 series, we explored the sensitivity of our results to the refractive index of the haze ices, the tropospheric methane cloud's optical depth, the cloud top pressure, the single-scattering phase function of the cloud particles, the mixing ratio profile of gaseous methane, and the eddy mixing coefficient in the lower stratosphere.

In fitting the various models to the high phase angle, wide-angle camera data, we found that two solutions were possible. One solution, which we term the "low density" solution, was characterized by a mean particle radius of 0.13 ± 0.02 μm and a number density of 1–3 particles/cm^3 at a reference pressure level of 44 mbar and a total mass production rate of 2- to 15×10^{-17} g/cm^2/s. The alternative solution, the "high-density" solution, was characterized by particles having 0.6–0.7 times the size, one hundred times the number density, and ten times the total mass production rate of the low-density solution. The particles of the high-density solution were also more highly charged than those of the low-density solution. As discussed in more detail in the next section, the production rates required by the low-density solutions are consistent with those that can be plausibly derived by photochemical pro-

TABLE 3. Wide-Angle Images: Geometry and Specific Intensities

Filter	Phase Angle Cosine	Emission Angle Cosine	Incidence Angle Cosine	Observed I/F	Calculated[a] Best Fit	Rayleigh–Raman-CH4	Particle Size[b]		Number Density[c]	
							/2	×2	/2	×2
WA violet	156.9	0.094	0.294	0.532	0.544	0.451	0.450	1.074	0.499	0.626
	152.8	0.163	0.296	0.468	0.480	0.416	0.414	0.785	0.448	0.538
	147.9	0.239	0.282	0.393	0.404	0.364	0.363	0.554	0.384	0.440
WA blue	157.3	0.089	0.282	0.543	0.541	0.436	0.436	1.156	0.492	0.628
	152.8	0.165	0.285	0.480	0.469	0.395	0.399	0.809	0.437	0.528
	148.0	0.241	0.294	0.421	0.413	0.361	0.368	0.583	0.393	0.451
WA green	157.5	0.089	0.280	0.560	0.538	0.398	0.431	1.219	0.495	0.610
	152.9	0.160	0.288	0.486	0.477	0.354	0.401	0.859	0.452	0.523
	148.0	0.239	0.305	0.423	0.416	0.318	0.357	0.600	0.400	0.445
WA orange	157.1	0.090	0.274	0.507	0.526	0.371	0.423	1.154	0.491	0.587
	152.9	0.160	0.289	0.462	0.474	0.327	0.394	0.837	0.454	0.512
	148.0	0.237	0.284	0.389	0.385	0.278	0.321	0.559	0.372	0.409

[a]Specific intensities for haze model US8 with the free parameter values given in Table 5.
[b]Specific intensities for haze model US8 with particle sizes half and twice those of the best fit, respectively.
[c]Specific intensities for haze model US8 with number densities half and twice those of the best fit, respectively.

cesses, whereas the production rates required by the high-density solution cannot plausibly be obtained by photochemistry. We therefore have focused much of our attention on the low-density solutions.

Table 5 summarizes the parameters obtained by matching the various models of Table 4 to the wide-angle imaging data of Table 3. From left to right, this table contains the name of the model, the type of solution (low or high density) and information on nonstandard parameter choices, the best fit scaling parameters SR and SN, the modal size r_m and number density n at the reference pressure level of 44 mbar, the mass production rate dM, and the particle charging Q, together with their associated error bars. To derive the best fit values of r_m and n, we simply multiplied the values of these parameters for the model of interest by the scaling factors SR and SN, obtained by fitting it to the data. Typically, SR and SN had values that lay between 0.8 and 1.2, and 0.7 and 1.8, respec-

tively. However, SR and SN had values of about 0.5 and 100, respectively, for the high-density solution of a nominally low-density, microphysical model. We therefore constructed two high-density microphysical models (US 17 and 26) to obtain better defined parameter values for the high-density solutions.

The best fit values of dM and Q were derived from the nominal values of these parameters for a given model and the best fit scaling factors, SR and SN. For this purpose, we used a first-order Taylor series expansion:

$$\ln (n/n_0) = \ln (SN) = a_n \ln (Q/Q_0) + b_n \ln (dM/dM_0) \quad (5)$$

$$\ln (r_m/r_{m0}) = \ln (SR) = a_r \ln (Q/Q_0) + b_r \ln (dM/dM_0) \quad (6)$$

In the above equations, ln means logarithm to the base e, unscripted variables refer to the best fit values, and variables with subscript 0 refer to values given by the baseline microphysical model. The four linear coefficients in the above

TABLE 4. Properties of the Microphysical Models

Name	Shape	Relative Production Rates	dM, 10^{-17}g/cm^2/s	Q, 10^{-5}esu/cm	r_m, μm	n, per cm^3
US 5	S	3, 17, 80	11	0	0.145	1.3
US 8	S	50, 10, 40	8.9	0	0.135	1.5
US 17	S	3, 17, 80	76	14	0.075	140
US 18	S	75, 5, 20	8.9	0	0.135	1.5
US 20	S	100, 0, 0	8.9	0	0.135	1.6
US 26	S	100, 0, 0	59	11	0.075	140
US 32	S	20, 40, 40[a]	7.3	0	0.13	1.4
UF 10	FD	3, 17, 80	8.2	5.5	0.16	1.4
UF 19	FD	100, 0, 0	4.1	4.8	0.145	1.2
UF 20	FD	5, 30, 65	8.2	5.5	0.155	1.6
UE[b]	FD	3, 17, 80	8.2	5.5	0.15	1.8

Two particle shapes were considered: spheres (S) and flat disks (FD). The thickness of the flat disks was 0.1 times the radius. Relative production rates are given as percentages of the total rate for the regions where diacteylene, acetylene, and ethane condense, respectively. Parameter dM is the total mass production rate, Q is the particle charge per unit length, r_m and n are the modal particle radius and number density at a pressure level of 44 mbar. A value of Q of 5×10^{-5} esu/cm (electrostatic units per centimeter) corresponds to one electron per 0.1 μm radius. In the case of the flat disk models the modal radius is that of an equal-volume sphere.

[a]Except for model US 32 the ice condensation regions are those given in Table 2. For model US 32, the acetylene condensation region was altered to lie between 1 and 2.4 mbar, while the other two regions were kept the same as in Table 2.

[b]The eddy diffusion coefficients were enhanced by a factor of 100 over their nominal values between 1 and 20 mbar, while remaining the same as the nominal values elsewhere.

TABLE 5. Best Fit Parameter Values for the Microphysical Models

Model	Nonstandard Values[a]	SR	SN	r_m, μm	n, per cm³	dM, 10^{-17} g/cm²/s	Q, 10^{-5} esu/cm
US 5		0.85(0.06)	1.7(0.66)	0.123(0.009)	2.2(0.8)	4.2–15.4	1.1–3.9
US 8		0.88(0.07)	1.8(0.74)	0.119(0.009)	2.6(1.1)	3.8–15.9	1.1–4.0
US 8	HDS	0.53(0.02)	100(41)	0.072(0.002)	145(59)	16.8–49	20–23
US 17	HDS	1.04(0.03)	1.4(0.65)	0.078(0.003)	194(90)	62–187	13–17
US 18		0.93(0.08)	1.3(0.59)	0.126(0.01)	2.0(0.8)	3.3–16	0–2.6
US 20		0.94(0.09)	1.25(0.56)	0.127(.012)	1.9(0.9)	3.3–16.7	0–2.3
US 26	HDS	1.2(0.02)	1.0(0.42)	0.09(0.002)	138(58)	75–185	8.1–12
US 32		0.94(0.08)	1.5(0.65)	0.122(0.011)	2.1(0.9)	3.4–15.3	0–3.1
UF 10		0.88(0.07)	1.06(0.41)	0.141(0.011)	1.5(0.6)	2.3–9.8	5.8–6.2
UF 10	$p = S$	0.94(0.10)	0.73(0.37)	0.15(0.016)	1.0(0.5)	1.5–10.6	5.0–5.5
UF 10	$p = I$	0.96(0.16)	0.80(0.62)	0.154(0.025)	1.1(0.9)	2.0–11.8	5.5–5.8
UF 10	P_c	0.94(0.08)	0.80(0.32)	0.15(0.013)	1.1(0.5)	2.1–9.9	5.2–5.6
UF 10	τ_c	0.88(0.07)	1.15(0.43)	0.141(0.011)	1.6(0.6)	2.5–10.5	5.9–6.3
UF 10	$C = 3$	0.88(0.08)	1.1(0.49)	0.141(0.013)	1.5(0.7)	2.0–11	5.8–6.2
UF 10	$C = 1.9$	0.90(0.07)	0.95(0.40)	0.144(0.011)	1.3(0.6)	2.1–9.8	5.5–6.0
UF 10	C, n_r	0.83(0.07)	0.95(0.35)	0.133(0.011)	1.3(0.5)	1.6–6.9	5.9–6.2
UF 10	C, HDS	0.51(0.02)	100(30)	0.082(0.003)	140(42)	31–79	22–24
UF 10	I, HDS	0.49(0.01)	85(22)	0.078(0.002)	119(31)	25–51	8.1–23
UF 19		0.95(0.09)	1.4(0.69)	0.138(0.013)	1.7(0.8)	1.6–10	5.7–6.3
UF 20		0.94(0.09)	1.25(0.56)	0.127(0.012)	1.9(0.9)	2.9–16.7	5.7–6.1
UE		0.90(0.10)	0.90(0.46)	0.135(0.015)	1.7(0.8)	1.5–11.1	5.4–5.9

SR and SN are the scaling factors for particle size and number density, respectively; r_m and n are the modal radius and number density at 44 mbar; dM is the total mass production rate; and Q is the particle charge per unit length. Q equal to 5×10^{-5} corresponds to one electron per 0.1 μm radius. In the case of the flat disk models the modal radius is that of an equal-volume sphere. The values in parentheses are 1 standard deviation uncertainties. For the flat disk particle models the coefficients a_n, b_n, a_r, b_r of equations (5) and (6) had values of 2.67, 0.439, -0.654, and 0.139, respectively. The corresponding coefficients for the spherical particle models and a slightly modified form of these equations (see text) were 2.03 $\times 10^4$, 0.198, -4.10×10^3, and 0.196, respectively.

[a]The nonstandard values are as follows. HDS means high-density solution; $p = S$ and $p = I$ correspond to the use of a Saturn cloud phase function and an isotropic phase function, respectively, for the methane cloud particles. Note that the $p = I$, low-density solution gave much larger residuals; i.e., it was a poorer fit, than the low-density solution for $p = S$ or the standard Jupiter phase function. P_c and τ_c refer to models in which the methane cloud top pressure was increased from 0.9 to 1.05 bars and the optical depth of this cloud was increased from 0.45 to 0.9, respectively. $C = 3$ and 1.9 correspond to methane mixing ratios of 3 and 1.9%, respectively, below the methane cloud (see text for further details). C corresponds to the 1.9% case. Parameter n_r refers to a case where the real index of refraction of the stratospheric aerosols was set equal to 1.65, rather than the indices given in Table 2. Finally, I corresponds to the isotropic phase function for the methane cloud particles.

equations, a and b, were obtained by fitting them to a limited number of runs with the microphysical model, for which dM was systematically varied with Q held constant, and vice versa. The above equations were used for the UF series, while Q rather than ln (Q) was used for the US series, since Q was 0 for many of the microphysical models of this series. Values for these coefficients are given in a footnote to Table 5. By inverting these equations, we readily obtained the best fit values of dM and Q.

According to Table 5, the best fit values of r_m, n, and dM for a given type of solution are very insensitive to the values chosen for the relative production rates of stratospheric ices, the refractive index of the stratospheric aerosols, their shape, the eddy mixing coefficient profile in the condensation region, methane cloud properties, and the profile of gaseous methane. These values are, of course, quite different for the two types of solutions. The best fit charge of the particles depends both on the shape of the particles and the type of solution but is insensitive to all the remaining parameters. For a given microphysical model and type of solution, the best fit values of r_m can be determined to an accuracy of about 5–10%, while uncertainties of 30–50% characterize the best fit values of n.

Although the best fit values of the stratospheric ice properties were insensitive to the choice of the single-scattering phase function of the methane cloud particles, the goodness of the fit to the observed brightnesses was affected by this choice. In

particular, much larger variances characterized the low-density solutions with an isotropic phase function than those with strongly forward-scattering ones. The isotropic, low-density solution for model UF 10 had single-point deviations of about 5% in the relative specific intensities at different phase angles for a given filter, as compared to values of about 1% for the more forward scattering cases and an uncertainty of about 1% in the observed relative intensities.

A further indication of our ability to deduce the values for these parameters is given in Table 3. The I/F values derived for a low-density solution of model US 8 are shown and compared with the observed I/F values. Also shown in this table are the I/F values that result when the modal particle size of the best fit model is alternately increased and decreased by a factor of 2 and when a similar exercise is performed with the best fit number density.

The fits of the models to the observed brightnesses have also resulted in a crude estimate of the imaginary index of refraction of the stratospheric ice particles at a wavelength of 0.55 μm. We find that this index lies between 0.005 and 0.02. It was not possible to obtain a useful value for the wavelength dependence of this index from the high phase angle data. Much better constraints on this parameter will be obtained from our forthcoming analyses of the low phase angle images (K. Rages et al., manuscipt in preparation, 1987).

Figures 4a, 4b, 4c and 4d illustrate the vertical profiles of
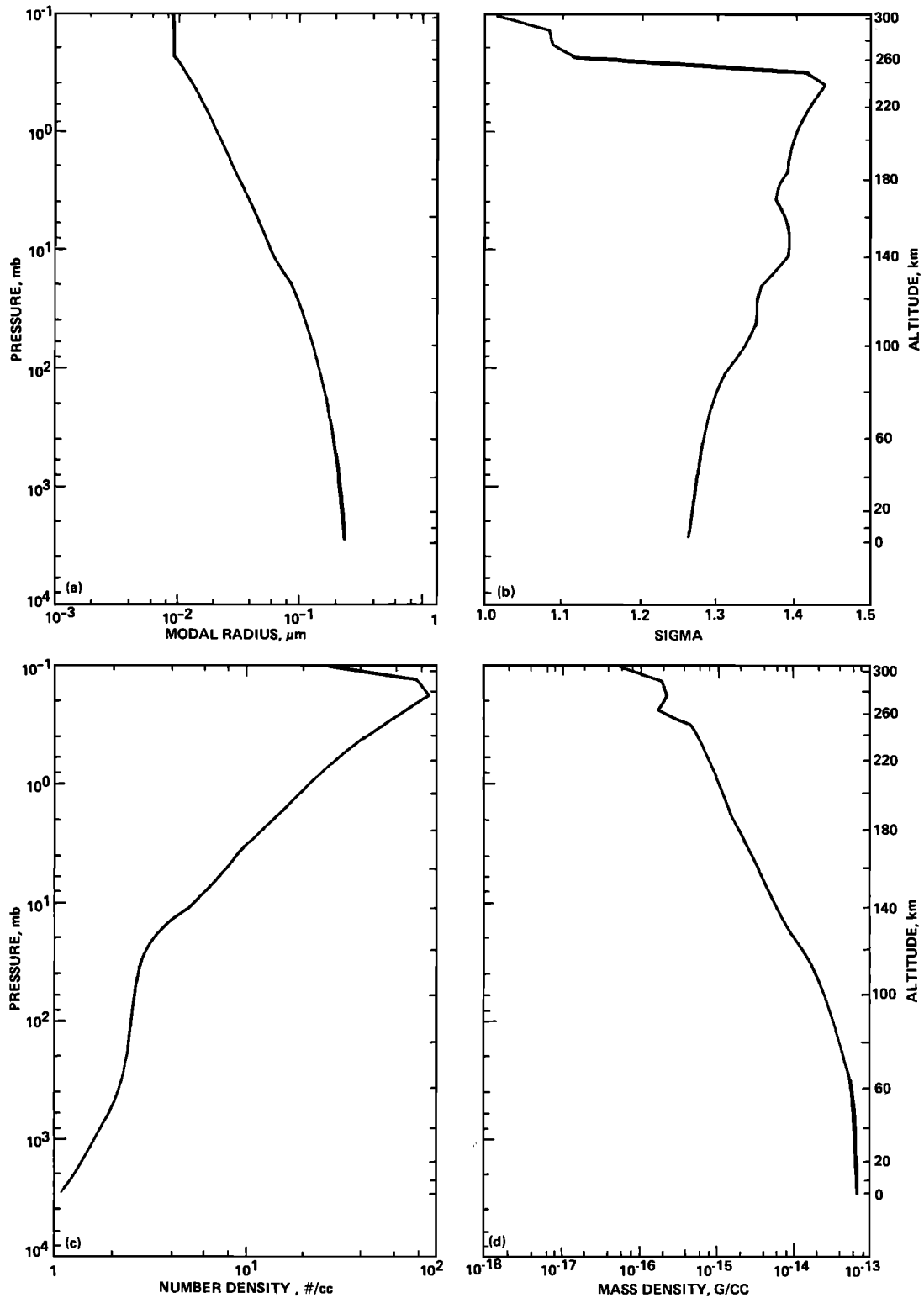
Fig. 4. Haze properties of model US 8 as a function of pressure. These model results have been obtained after scaling the modal particle radius and number density by scale factors of 0.88 and 1.8, respectively, as indicated by the Voyager image analysis. (a) Modal radius, (b) width, σ, of the size distribution, (c) number density, and (d) mass density.

the modal particle radius, width of the size distribution, σ, number density, and mass density of microphysical model US 8, after multiplying its properties by the scaling factors derived from the Voyager data. As we will see in the next subsection, this model produces an acceptable fit to the limb data. Its properties are typical of most other microphysical models for

the low-density solution that fit the limb data. The profiles of Figure 4 extend from a pressure level of 0.1 mbar, where diacetylene first condenses, to the base of the stratosphere at a pressure of about 150 mbar, down through the upper troposphere to a pressure of several bars. At pressures in excess of about 400 mbar, the profiles shown in Figure 4 are probably

in error owing to the evaporation of the more volatile ice species and an enhanced eddy mixing. These effects will be discussed in the next section of this paper.

3.2. Narrow-Angle Images

Using the spherical geometry program described in section 2.2, we have inverted narrow-angle images of the planet's limb to obtain the extinction coefficient as a function of altitude. This inversion was performed on images obtained at phase angles of 148°, 153°, and 157° through the green and clear filters. These images pertain to a latitude of approximately 25°.

The circles of Figures 5a and 5b show the retrieved total extinction profiles for the green and clear images at a phase angle of 157°. Very similar results were obtained at the other phase angles. These extinction coefficients refer to the sum of molecular Rayleigh scattering and aerosol scattering. The extinction profile shown as circles in Figures 5a and 5b was obtained by fitting the limb radiance profile close to its peak brightness to derive a value of the product of the total (gas plus aerosol) single-scattering albedo ϖ_0 and phase function p and by assuming that this product was independent of altitude.

The pressure scale on Figure 5 has been set by employing the parameters of model US 8, as described in section 2.2. The pressure normalization point is shown by the cross inside the circle. This point lies close to an altitude at which the slant path optical depth is unity in the wide-angle images used to determine the parameters of model US 8. The dashed curve shows the extinction coefficient due solely to Rayleigh scattering. It lies noticeably below the deduced total extinction (circles) at levels having pressures in excess of 5–10 mbar. Thus aerosols are present throughout the lower stratosphere, in rough qualitative agreement with the predictions of the photochemical model.

The solid line in Figure 5 shows the total extinction predicted by the best fit to model US 8. It lies close to the inversion profile. So far, we have ignored the variation of aerosol scattering properties with altitude, as occur in all of our microphysical models. To carry out a more precise comparison of the predictions of various best fit models with the inversion results, we need to allow for these variations. In addition, it is useful to remove the molecular scattering component. For this purpose, we followed the protocol of Appendix B. Using the single-scattering characteristics of a given microphysical model, we derived a vertical profile for the "haze scattering parameter" defined in the last equation of the appendix. This theoretical profile was compared with the "observed" profile of the haze scattering parameter, deduced by subtracting the molecular component from the inversion result. For each best fitted model, the Rayleigh component is known. The equations of Appendix B are valid in places where the slant path optical depth is less than unity.

Figures 6a and 6b show such a comparison for model US 5, which has been scaled by the best fit, low-density solution to the wide-angle images. The particles are equidimensional for this model, and the relative production rates of ices in the three condensation regions are in accord with the values suggested by the nominal photochemical model: 3, 17, and 80% in the condensation zones of diacetylene, acetylene, and ethane, respectively. The solid line and its associated stippling in Figure 6a denote the observed profile for the haze scattering parameter and its estimated uncertainty for the clear filter image taken at a phase angle of 157°, while the corresponding

line and stippling in Figure 6b refer to the 157°, green filter image. These profiles are typical of those obtained at other locations on these images. The model profile for the haze scattering parameter is shown by the dashed curve in these figures.

While the model profiles closely track the observed ones at pressures larger than 15–20 mbar, they fall significantly below the observed curves at pressures ranging from several to 15 mbar. At pressures lower than a few millibars, the observed profile is ill defined. Thus model US 5 does not give a satisfactory fit to the narrow-angle, limb images.

In performing comparisons between the observed and theoretical profiles of the haze scattering parameter for the other models of Table 4, we have found that the goodness of fit is determined chiefly by the relative ice production rates. In particular, enhancing the relative rates in the diacetylene condensation region or in both the diacetylene and acetylene condensation regions leads to much better fits, as illustrated in Figures 6c, 6d, 6e, 6f, 6g, and 6h for low-density models having spherically shaped particles (models US 8, 20, and 32). Changing the pressure boundaries of the ice condensation regions by factors of several had much less of an impact on the goodness of the fit.

For models having enhanced production aloft the model profile of the haze scattering parameter agrees with the observed profile for the clear filter to within the uncertainty of the latter (cf. Figure 6). While the theoretical profiles of these models lie much closer to the observed profile for the green filter than does the profile of model US 5, they still are not in good agreement for pressures ranging from several to 15 mbar. We suspect that part of this disagreement stems from the poorer effective resolution of the green filter image, whose exposure time was a factor of 4 larger than that of the clear filter image. A combination of spacecraft motion and limit cycle motion may have degraded the effective resolution of the green filter image by about a factor of 2, from the intrinsic resolution of 11 km/line pair (lp), while affecting the clear filter image much less severely. At levels where the intrinsic profile decreases steeply and has noticeable curvature, smear could have led to somewhat larger values of the haze scattering parameter (cf. Figure 6d). Thus the fits of the models with enhanced production aloft to the green filter profile may be acceptable, within the resolution limitations of this image.

Figures 7a–7h show comparisons between the theoretical and observed profiles of the haze scattering parameter for two low-density models with highly flattened disks (UF 10 and 19) and two high-density models, with spherical particles. As for the low-density models with spherical particles, models with enhanced production aloft provide much better fits to the data.

Finally, Figures 8a and 8b compare the observed profiles of haze scattering parameter with those of a model having greatly increased eddy mixing coefficients between 1 and 20 mbar (model UE). Otherwise, this model is nearly identical to model UF 10 in having most of the production occurring in the ethane condensation zone. This model produces a fit to the data comparable to that of the models with enhanced production aloft.

4. DISCUSSION

4.1. Evidence for Condensed Hydrocarbons

The results of this paper, in conjunction with other Voyager data, provide evidence that the stratospheric haze on Uranus
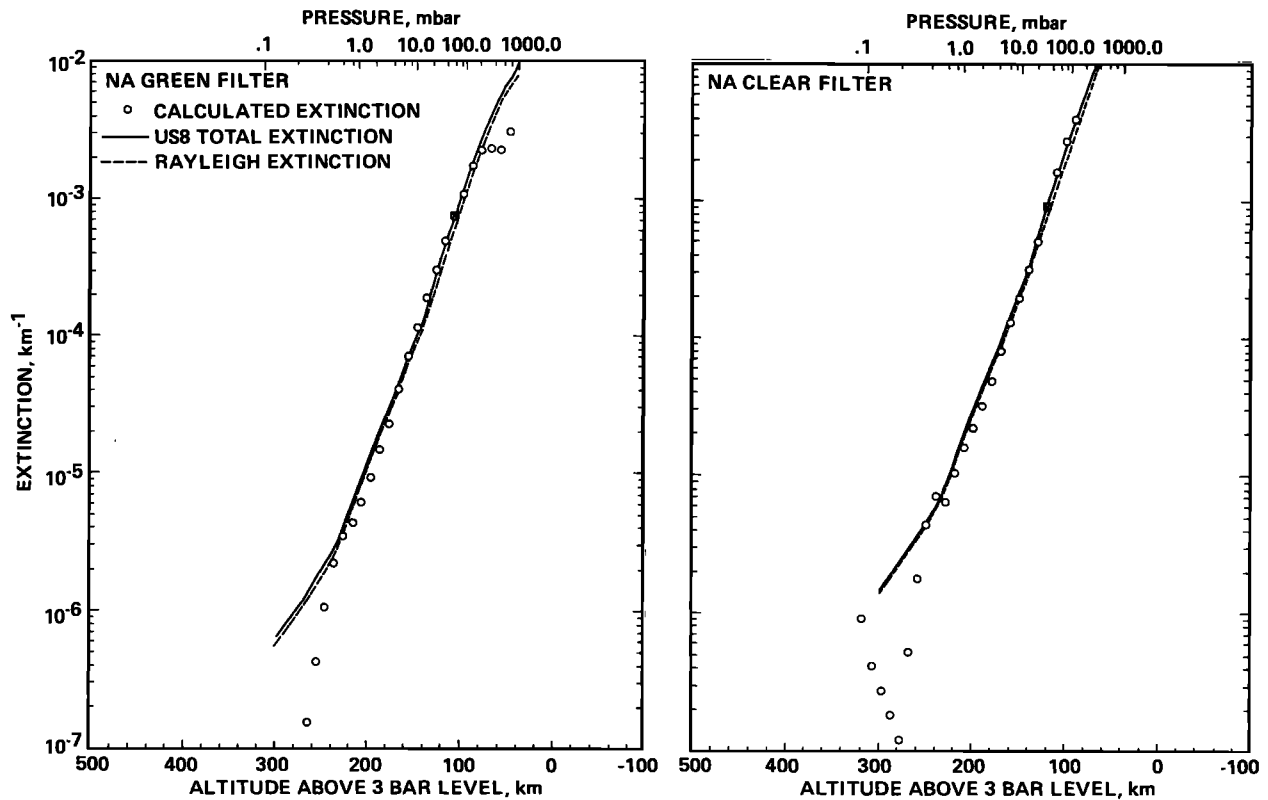
Fig. 5. Total extinction coefficient as a function of pressure for (a) a narrow-angle green image at a phase angle of 157° and (b) a narrow-angle clear image at the same phase angle. The meaning of the various symbols and curves is explained in the text.

is formed, at least in part, from the condensation of lower-order hydrocarbons in the planet's lower stratosphere. Below, we review this evidence.

On strictly theoretical grounds, there is strong reason for suspecting that ethane, acetylene, and diacetylene, produced in the upper stratosphere by methane photolysis, condense in the lower stratosphere and are major sources of the stratospheric haze [Atreya and Ponthreu, 1983; Atreya and Romani, 1985; Romani and Atreya, 1986]. Given the constraints imposed on the eddy mixing coefficient in the stratosphere by the Voyager UVS experiment, one can calculate fairly precisely the mixing ratio profiles of the lower-order hydrocarbons. This expectation is based on the success of comparable calculations for Jupiter and Saturn, where the observed mixing ratios of methane, ethane, and acetylene can be reproduced to within a factor of about 2 [Atreya, 1984]. Given these profiles and the temperature structure of the lower stratosphere of Uranus measured by Voyager [Tyler et al., 1986; Lindal et al., this issue], it is inevitable that ethane, acetylene, and diacetylene condense in the stratosphere. Furthermore, owing to the very low temperatures near the Uranian tropopause, alternative precursor gases for forming stratospheric hazes, such as NH_3 and PH_3, are expected to have much too low a mixing ratio in the Uranian stratosphere for their photolysis products to have comparable abundances to that of the lower-order hydrocarbons [West et al., 1986].

The results of section 3 of this paper provide further support for the Uranian stratospheric hazes being formed by the condensation of lower-order hydrocarbons, and they may have interesting implications for the photochemistry. The results of particular relevance are the constraints on the relative production rates in the three condensation zones, derived from

the analysis of the narrow-angle images, and the estimates of the total mass production rate, derived from the analysis of the wide-angle images. The nominal photochemical model predicts that 3, 17, and 80% of the total condensation rate occurs in the regions where diacetylene, acetylene, and ethane condense, respectively. Most microphysical models having these relative production rates (e.g., US 5, UF 10, and US 17) predict profiles for the haze scattering parameter of Appendix B that differ substantially from the observed ones (cf. Figures 6, 7, and 8).

There are three possible solutions to the above discrepancy. First, the eddy diffusion coefficient may be enhanced by several orders of magnitude in the lower stratosphere, owing, say, to the radiative effects of the condensed ice. Although the radio occultation temperature profiles exhibit noticeable structure in the 1- to 20-mbar region [Lindal et al., this issue], as discussed further below, such a large increase in the eddy diffusion coefficient throughout this region seems unlikely to us, based on the overall strong static stability here and experience with the stratospheres of Jupiter and Saturn [Atreya, 1984].

A second possible solution to the discrepancy in the vertical profiles is to invoke the influence of systematically directed vertical velocities due to the general circulation of the atmosphere. These velocities could be important if they are comparable to or larger than the ice particles' sedimentation velocities. Values for the sedimentation velocity of modal sized particles of model US 8 are given in Table 6. Values for most other models are comparable to these. Thus, if the atmospheric winds have vertical velocities of the order of 10^{-2} cm/s or greater in the lower stratosphere, they could exert an impor-
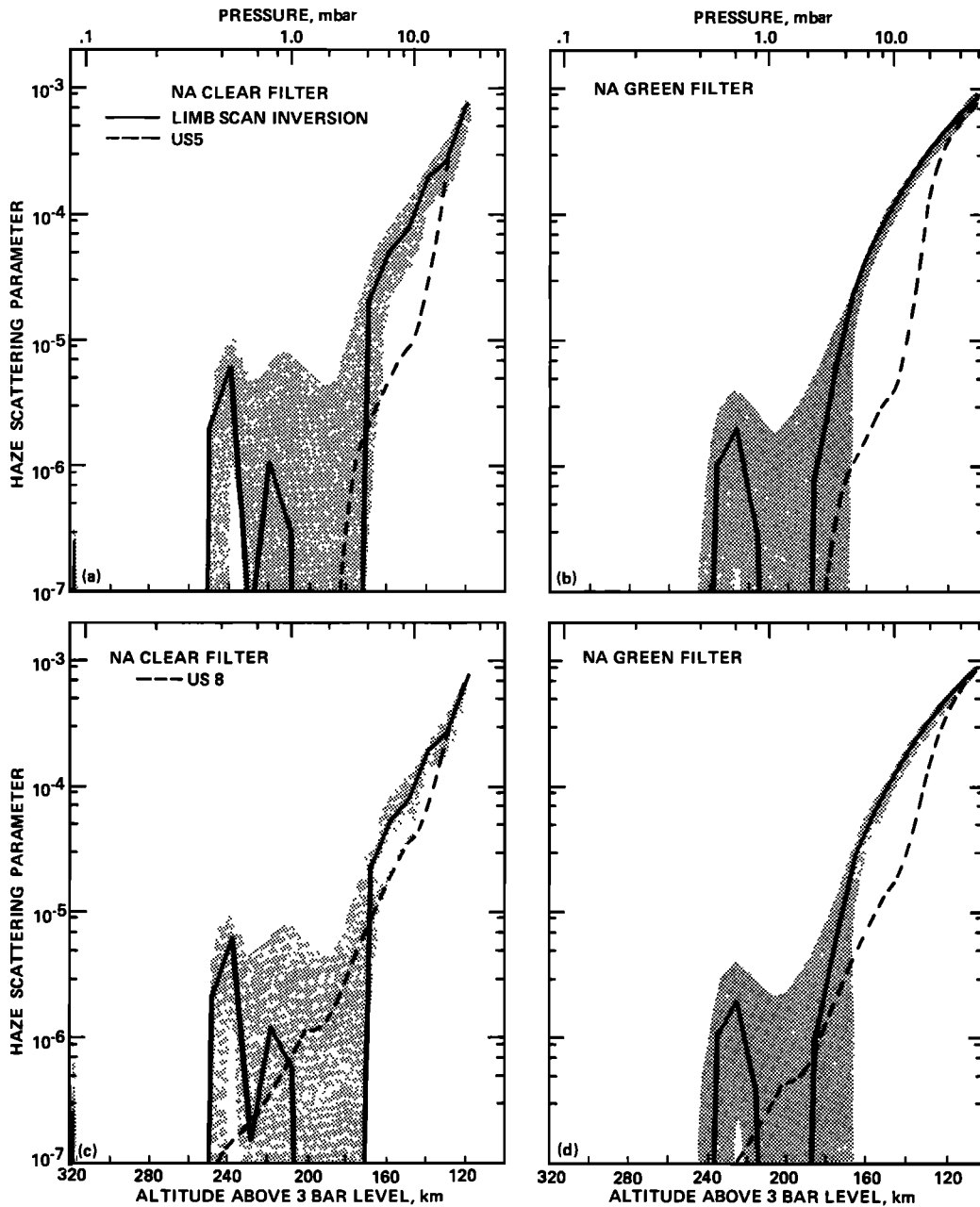
Fig. 6. Comparison of the profile of the haze scattering parameter of Appendix B (solid curve) and the profile of this parameter predicted by a Voyager-fitted, microphysical model. The stippling indicates the estimated uncertainty in the inversion values. These figures are for the low-density solutions for the spherically shaped particle models US 5, US 8, US 20, and US 32. Properties of these models are given in Table 4. For each model, first, comparisons are made for the clear filtered image and next, for the green filter image.

tant influence on our microphysical models. Lacking relevant wind estimates, we have not explored this possibility. However, simply scaling the zonal velocities measured by the Voyager imaging experiment by the ratio of the scale height to the planetary radius (steady state mass conservation) indicates that the vertical velocities could easily be large enough to be important. This matter deserves further study.

A third possible solution is to enhance the relative production rates in the regions where diacetylene and acetylene condense. According to Figures 6, 7, and 8, the sum of the relative rates in these two regions needs to be increased to at least 50% of the total rate, i.e., by at least a factor of 2.5 above

the nominal value. Such increases are possible for several reasons. First, the uncertainty in the predicted relative rates is a factor of about 2, due to uncertainties in the gas kinetics and the eddy diffusion profile. On this basis alone, it would be possible to alter the relative rates of acetylene and ethane condensation to ones of near parity. Also, it is likely that the pressure at which acetylene begins to condense is smaller than the value given in Table 2. This effect would somewhat elevate the acetylene ice production rate, as discussed in section 2.3. Second, the calculation of condensation rates is based solely on the diffusion of gases from their photochemical production regions to their condensation levels. In the case of ethane and
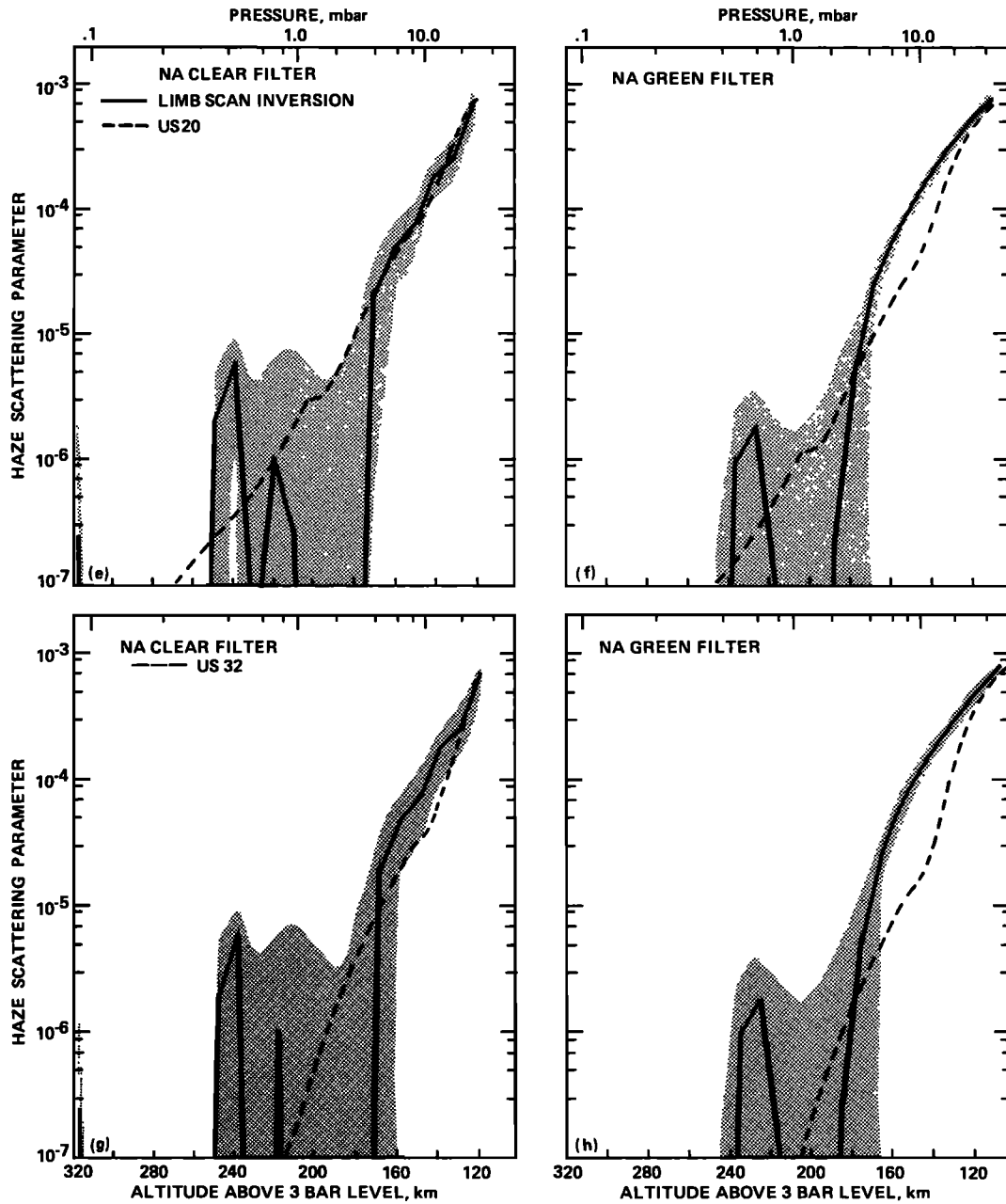
Fig. 6.   (continued)

acetylene, this is probably a reasonable procedure, since the two sets of levels are well separated from one another. However, there is a significant overlap of these levels in the case of diacetylene, as illustrated in Figure 1. This raises the possibility that production and condensation of diacetylene gas occur at common levels in the atmosphere. If so, the diacetylene condensation rate could be significantly augmented over that given in Table 2, since a substantial fraction of the diacetylene gas produced from acetylene gas is recycled back to acetylene in the absence of concurrent condensation.

We have obtained crude estimates of the production rate of diacetylene ice that is possible when allowance is made for concurrent production of the gas and its condensation. Equating the production rate of the ice to the production rate of the gas in regions where the condensation rate of the vapor onto preexisting tiny ice particles exceeds the production rate of

gaseous diacetylene, we find a production rate of diacetylene ice of about 1.5×10^{-17} g/cm²/s, i.e., a value comparable to the production rate of ethane ice. If diacetylene ice were to be produced at the same rate as its precursor gas throughout the stratosphere, a highly unlikely situation, this rate would be an order of magnitude larger than the number quoted above. We conclude that the vertical profiles of the aerosol parameter derived from the narrow-angle images are consistent with those expected from the condensation of lower-order hydrocarbons in the lower stratosphere if a significant fraction of the ice is derived from the condensation of diacetylene and acetylene, as is quite plausible.

Analyses of the wide-angle images led to two possible ranges of values for the total aerosol production rate. The low-density solutions led to values lying between about 2 and 15×10^{-17} g/cm²/s, while the high-density solutions led to
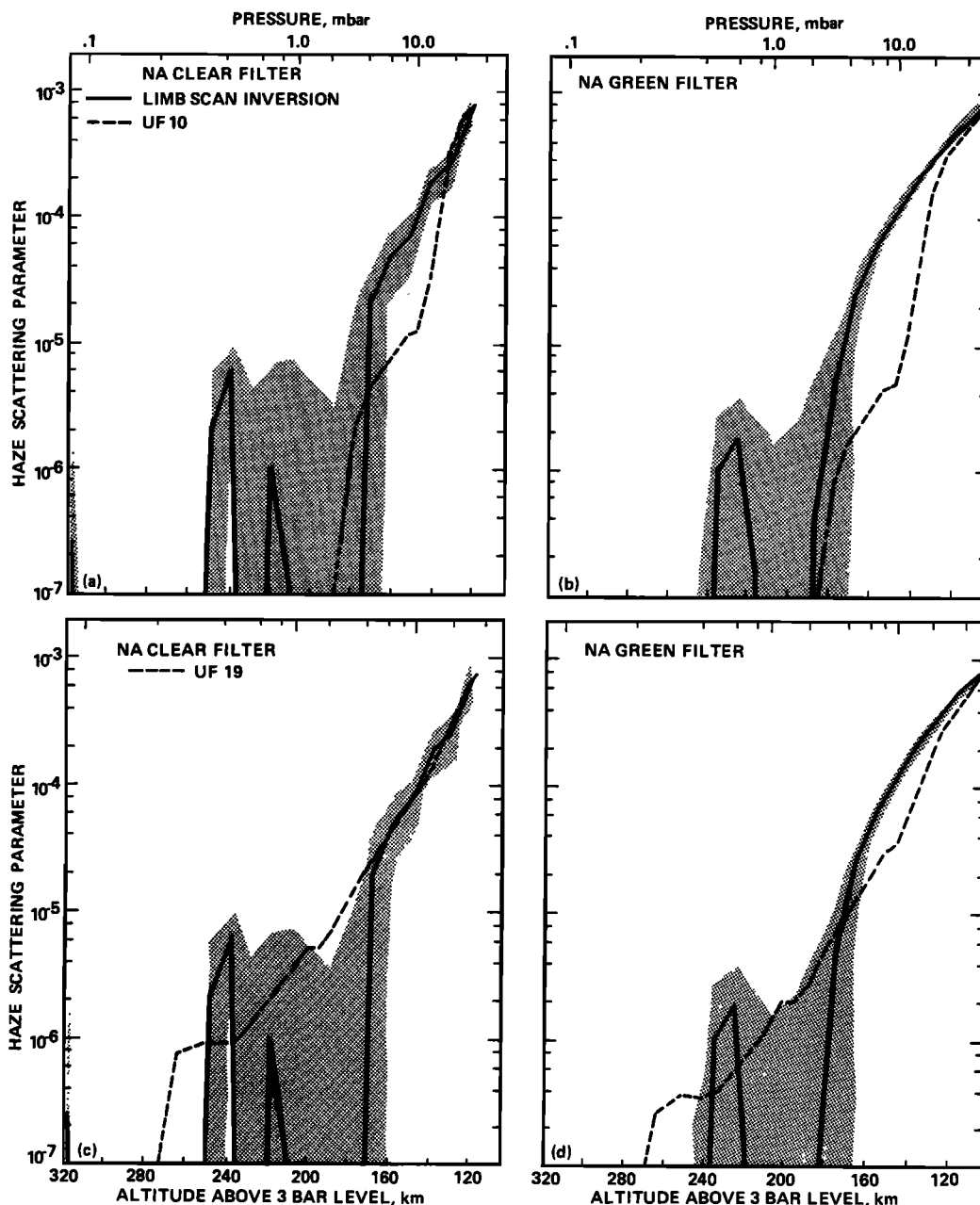
Fig. 7.   Same as for Figure 6, but for the thin-disk models UF 10 and 19 for the low-density solution and spherical models US 17 and 26 for the high-density solutions.

values that were an order of magnitude larger. According to the results presented in the second section of this paper, the nominal photochemical model predicts total condensation rates that lie between 1.25 and 5×10^{-17} g/cm²/s. When allowance is made for the augmented rate of diacetylene condensation discussed above, this upper bound could plausibly be raised by as much as a factor of 2. Thus the low-density solutions are consistent with the predictions of the photochemical model, while the high-density solutions are not.

Precipitation of magnetospheric high-energy electrons into the auroral regions of Uranus provides an additional energy source for producing gaseous and solid hydrocarbons [*Thompson et al.*, this issue; *Khare et al.*, this issue]. Scaling their laboratory experiments to Uranus, *Thompson et al.* [this

issue] estimate that the globally averaged production rate of gaseous hydrocarbons by precipitated magnetospheric electrons equals about 0.1 times the production rate by solar UV photolysis of methane. The globally averaged production rate of heavy hydrocarbons (C_6 or higher) by the magnetospheric source is about 10^5 C/cm²/s or about 2×10^{-18} g/cm²/s [*Thompson et al.*, this issue]. This rate provides a crude estimate of the rate at which solid aerosols are generated by this mechanism [*Khare et al.*, this issue].

It should be noted that the above estimates are based on experiments in which the methane-mixing ratio had a value of 1.2×10^{-3} and the pressure had a value of 57 mbar. The methane-mixing ratio and the pressure at the levels penetrated by magnetospheric electrons on Uranus are factors of 10^2–10^3
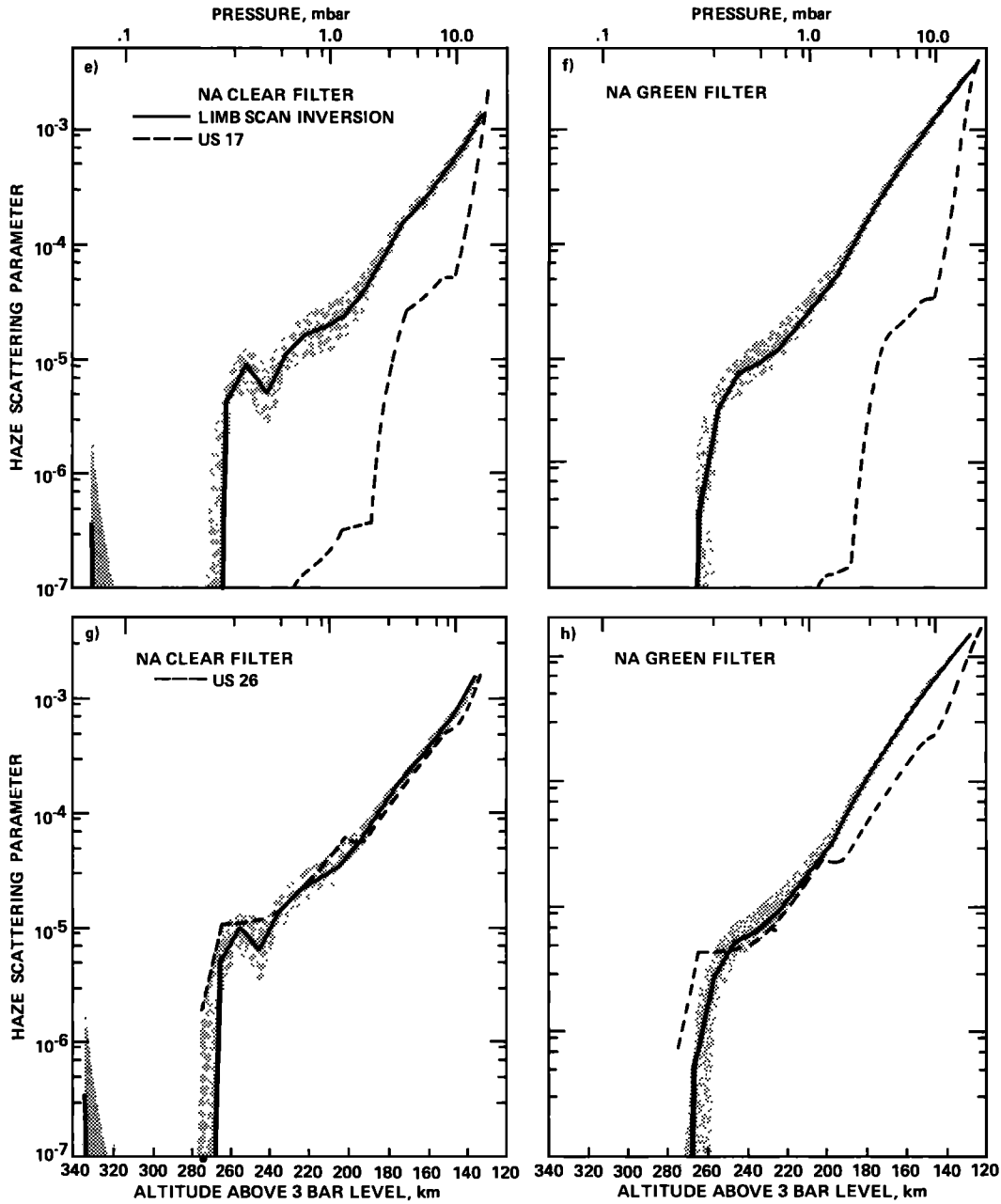
Fig. 7. (continued)

and 10^3–10^4 smaller than the above laboratory values. A re- duction in the methane-mixing ratio from the laboratory value will undoubtedly substantially reduce the above production rates, although a reduced pressure might somewhat elevate them [*Thompson et al.*, this issue]. Thus it seems very likely that solar UV photolysis provides the primary energy source for producing gaseous, lower-order hydrocarbons and haze material in the Uranian stratosphere. Therefore the inclusion of a magnetospheric source for the stratospheric haze will not alter our conclusion that the production rates required by the high-density solution are too high. In the next subsection we discuss the possible importance of the magnetospheric source for the visible absorbing component of the haze particles.

The temperature profile derived from the Voyager radio occultation experiment may provide additional support for the predictions of the photochemical model of *Atreya and*

Romani [1985]. Both the ingress and egress profiles, obtained close to the equator, exhibit noticeable deviations from a smooth monotonic behavior in the pressure range from about 1 to 20 mbar. A prominent local maximum in temperature occurs at a pressure level of about 15 mbar, which coincides closely with the pressure levels where most of the ethane is expected to condense (14–22 mbar). The other local maximum occurs at about 5 mbar, somewhat displaced from the region where most of the acetylene condensation is expected (2.5–3.5 mbar). However, the acetylene condensation level could be moved by a few millibars by plausible alternative choices in the canonical temperature profile used to calculate this level, as discussed in section 2.3. Although there is not enough of any of the lower-order hydrocarbons in the gas phase for their condensation to noticeably effect the temperature lapse rate through the release of latent heat, quite conceivably, the con-
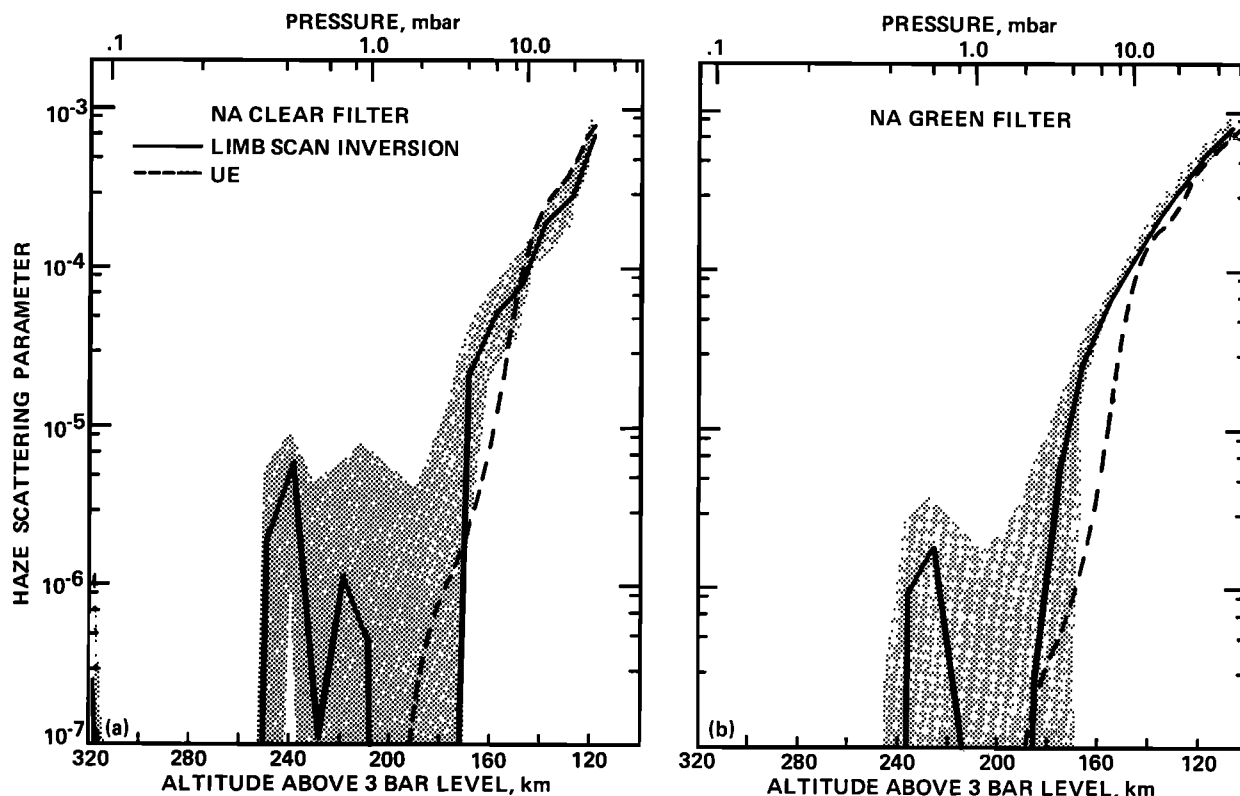
Fig. 8. Same as for Figure 6, but for the thin disk model UE for the low density solution.

densed ices could do so through their effect on solar radiation. This possibility needs to be further explored.

4.2. Aerosol Absorption

Although Uranus' geometric albedo is quite high in the visible region of the spectrum [*Neff et al.*, 1984], it is still measurably less than would be expected from a combination of molecular Rayleigh and Raman scattering [*Baines and Bergstralh*, 1986; *Pollack et al.*, 1986a]. This difference implies the existence of an absorbing aerosol component, whose continuum absorption coefficient declines from the near UV to the green region of the spectrum [*Pollack et al.*, 1986a].

Neither methane ice particles present near the 1-bar pressure level nor the low-order hydrocarbon ice species present in the lower stratosphere and upper troposphere are likely to supply the required visible absorption. To first approximation, the absorption bands in these ice phases are expected to occur at the same wavelengths as their gas species counterparts and to have similar absorption coefficients per mole to those of

TABLE 6. Time Constants

Process	Pressure, mbar	Time, years	Fall Speed, cm/s
Photochemical		5	
Gas transport	0.05–2.5	300	
Sedimentation	0.1	0.7	0.22
	1	2.6	0.043
	10	7.6	0.0095
	100	25	0.0026
	1000	84	0.0011
Dynamical (E-W)		0.05	
Dynamical (N-S)		1	

their counterparts [*Pollack et al.*, 1986a]. Thus, for example, methane ice is expected to exhibit little absorption longward of 0.15 μm, except in portions of the near infrared, where gaseous methane also absorbs. Even at the latter wavelengths, gaseous absorption is much more important than ice absorption [*Pollack et al.*, 1986a]. In a similar vein, ethane, acetylene, and diacetylene ices are not expected to strongly absorb longward of about 0.16, 0.20, and 0.27 μm, respectively.

One possible candidate for the visible aerosol absorber is higher-order hydrocarbons, which are produced in the gas phase by UV photolysis of methane. Their UV electronic absorption band might extend into the visible. However, the photochemical calculations reported in this paper suggest that the production rate for hydrocarbons of higher order than diacetylene is of the order of 10^{-3} of the total production rate. Even assuming that all of these species have an absorption coefficient in the visible comparable to that of polyethylene [*Podolak et al.*, 1984], we obtain a bulk imaginary index of refraction for the stratospheric ices of about 10^{-5} at a wavelength of 0.55 μm. Such a value appears to be too low by several orders of magnitude in comparison to that inferred from Uranus' visible brightness. For example, we inferred values of 0.005 to 0.02 from the high phase images, and crudely comparable values are obtained from analyzing the geometric albedo spectrum [*Pollack et al.*, 1986a, b].

Another possible source for the UV absorber is the production of higher-order hydrocarbons by solid state chemistry occurring in the lower-order hydrocarbon ices. The most likely energy source for this chemistry is solar UV radiation, since magnetospheric high-energy particles cannot penetrate to the depths where the aerosols are located and since there does not seem to be much lightning present in the Uranian atmosphere [*Smith et al.*, 1986]. Such solid state chemistry

would be expected to occur at the UV wavelengths where the absorption coefficient of the ices is not too small, i.e., the wavelengths at which the corresponding gas species absorbs, after taking account of any bathochromic shifts [Lombos et al., 1967]. Little solid state UV photolysis occurs in the tropospheric methane ice clouds. The overlying methane gas is optically thick, and the Rayleigh scattering optical depth is large enough to shield the cloud at wavelengths where the solid absorbs and the gas does not. However, relevant solar UV radiation (0.15 to 0.2 μm) can reach the altitudes where the hydrocarbon ices reside in the stratosphere. The hydrocarbon gases are not optically thick longward of about 0.15 μm, and the Rayleigh scattering optical depths for wavelengths between 0.15 and 0.2 μm are of the order of a few tenths at a pressure level of 100 mbar.

There is a limited amount of laboratory data concerning solid state chemistry that occurs in lower-order hydrocarbon ices when they are subjected to vacuum UV irradiation. Irradiation of acetylene ice by UV light at either 0.1236 or 0.1470 μm results in the production of molecular hydrogen gas [Stief et al., 1965]. In addition, a waxy residue was left behind when the irradiated ice was subsequently evaporated (L. J. Stief, private communication, 1987). The less hydrogenated, perhaps polymerized solid residue might absorb in the visible, by analogy to the absorption characteristics of polyethylene, polyacetylene, and graphite [Noy et al., 1979; Podolak et al., 1984]. Clearly, further laboratory experiments on the absorption properties of UV-irradiated ices would be highly desirable.

Still a third possible source for the absorbing component of the stratospheric haze is the complex hydrocarbons produced in the auroral zones by precipitating electrons [Khare et al., this issue]. Solid material produced in laboratory simulations has imaginary indices of refraction in the mid-visible that lie between 3×10^{-4} and 3×10^{-2} [Khare et al., this issue]. Since we find an imaginary index of 5×10^{-3} to 2×10^{-2} at 0.55 μm for the bulk stratospheric aerosols, the magnetospheric source would need to contribute more than several tens of percent of the haze material for it to be the chief visible absorber. It is not clear (see previous subsection) whether such a large contribution can be realized. Also, it is not clear whether winds would distribute the particles produced in the auroral zone fairly uniformly across the planet, as required by the planet's nearly constant brightness at visible wavelengths [Smith et al., 1986]. For these reasons, we tend to prefer solid state UV photolysis of the lower-order hydrocarbon ices as the source of the visible absorbing component of the haze, although the possible importance of the magnetospheric source needs to be examined further.

There is some evidence that the stratospheric haze absorbs long-wavelength UV and visible radiation. A preliminary analysis of the limb darkening of Uranus at a wavelength of 0.27 μm suggests that the single-scattering albedo of the aerosols is smaller at higher altitudes, in accord with a stratospheric source for the absorber [Lane et al., 1986]. The results of this paper also provide some evidence for the occurrence of significant absorption by the stratospheric aerosols at visible wavelengths.

4.3. Spatial Distribution

In this subsection we discuss the vertical extent of the stratospheric haze and its horizontal distribution. The hydrocarbon ice particles that are produced in the lower stratosphere gently fall under the influence of the planet's gravity into the troposphere. In the uppermost part of the tropo-

sphere, the temperatures are similar to those in the lower stratosphere, and the static stability is large, and so eddy mixing is small. Hence the aerosols at these altitudes can be expected to have properties very similar to those calculated with the microphysical model and shown in Figure 4a, 4b, 4c and 4d. However, at lower altitudes the more volatile ice species evaporate, and an enhanced eddy mixing, due to a lower static stability, tends to lower their number density. Also, the surviving ice species are probably incorporated into methane ice particles, especially in the 900- to 1300-mbar region, where the methane ice cloud is primarily located [Smith et al., 1986; K. Rages et al., manuscript in preparation, 1987].

We have estimated the evaporation levels in the troposphere for the various hydrocarbon ice species by comparing the mass densities predicted by the aerosol model with that obtained from their saturation vapor pressures. Total evaporation first occurs at the level at which these two mass densities are equal. The predicted mass densities of each hydrocarbon species were calculated in a straightforward manner from the total aerosol number density, size distribution, and relative mass production rate. The mass density of their saturated vapor was obtained from a combination of their vapor pressure curves and the perfect gas law. The former was specified by fitting analytic functions to measurements of the vapor pressures of ethane, acetylene, and diacetylene [Ziegler et al., 1964; Ziegler, 1959; Stull, 1947]. In this manner, we find that ethane, acetylene, and diacetylene ice evaporate at approximately the 600-, 900-, and 3000-mbar levels, respectively, for the low-density solutions and the relative production rates of Table 2. The temperatures at these locations are approximately 63, 72, and 100 K, respectively. Very similar results pertain to alternative choices of the relative production rates for ethane and acetylene ice, while even higher pressures and temperatures characterize a possibly much elevated relative production for diacetylene.

According to the above calculations, some of the mass of the stratospheric ice particles is evaporated before reaching the level at which the bulk of the methane ice cloud resides. However, both diacetylene ice and UV-altered ice species can be expected to persist throughout the altitude region inhabited by the methane ice clouds. These remaining stratospheric ice particles could serve as nucleation sites for the condensation of methane vapor. Because of both this and coagulation, the remaining stratospheric ice species are expected to largely be incorporated within methane ice particles in the region of the methane clouds. At the base of the methane cloud, methane ice particles evaporate, freeing the incorporated stratospheric material. The latter continue their journey into the deeper atmosphere, where they are eventually evaporated. Thus visible light absorbing material is expected to be present both within the methane clouds and in the region beneath them.

In the region from about 1 to 15 mbar, the aerosol properties are likely to be more complicated than and somewhat different from those obtained from the microphysical model and illustrated in Figures 4a, 4b, 4c, and 4d. Such a possibility is suggested by the complicated, oscillatory form of the Voyager radio occultation profile in this region [Lindal et al., this issue]. At both higher and lower altitudes, the occultation ingress and egress profiles are much smoother and tend to be much more nearly coincident. We suspect that the radiative interactions of the condensed hydrocarbon ice particles lead to a strong coupling of temperature lapse rates, vertical eddy mixing on local, vertical scales, and evaporation and condensation in the 1- to 15-mbar pressure region.

It is useful to define a number of characteristic time scales for assessing possible horizontal variations in the properties of the stratospheric haze. First, there are time scales associated with the formation of the precursor gases of the stratospheric ices and the transport of these gases from the upper to the lower stratosphere, where they condense. According to the photochemical calculations, approximately 3 to 6 years is required to reach a steady state distribution of lower-order hydrocarbon gases near the level of their peak production. Thus we can define a photochemical time constant τ_p, whose value equals the above numbers. This time scale indicates how long it would take the concentration of the lower-order hydrocarbons to change at the level of their peak production, when the incident solar UV is altered either as the result of geometry (seasonal effects) or solar output variations.

The transport time scale of these gases to the levels where they begin to condense can be obtained in a straightforward manner from the vertical distance L that they need to move and the average eddy diffusion coefficient for this path, K:

$$\tau_e = \frac{L^2}{K} \tag{7}$$

A representative value of τ_e for acetylene is 300 years. The corresponding time scales for diacetylene and ethane are somewhat smaller and larger, respectively, than this value for acetylene.

The time scale for the aerosols to move downward a distance L is controlled by their sedimentation or fall velocity, v_f. Thus this time scale is given by

$$\tau_f = \frac{L}{v_f} \tag{8}$$

If we set L equal to a gas scale height and use the modal particle size to define the fall velocity at a given altitude, then we obtain values for τ_f that equal approximately 0.7, 2.6, 7.6, 25, and 84 years at pressure levels of 0.1, 1, 10, 100, and 1000 mbar for model US 8. Comparable values hold for other acceptable models. The above estimates of time scales associated with haze production and dissipation indicate that the very slow rate of eddy mixing acts as the key control on the rate at which the haze properties vary with time. However, the amount of condensed diacetylene ice might vary on much shorter time scales if, as we suspect, in situ gas production and condensation play a major role for it.

We can define a dynamical time scale τ_d that provides an estimate of the time it takes an air parcel to get carried horizontally a distance L'' by the large-scale atmospheric winds. Let v be a characteristic velocity. The dynamical time scale is given by

$$\tau_d = \frac{L''}{v} \tag{9}$$

Using a typical value of 100 m/s for v in the east-west direction [Smith et al., 1986] and setting L'' equal to the planetary radius, we find that τ_d is approximately equal to about 0.01 years for transport around latitude circles. Thus there should be essentially no longitudinal variations in the haze properties. If v equaled a few meters per second in the north-south direction, as it seems to in the atmospheres of Jupiter and Saturn, τ_d would equal several years for transport between widely separated latitudes.

Finally, all the above time scales can be compared to the 84-year orbital period τ_0, over which there are very large changes in insolation at a given latitude. These variations are

URANUS' STRATOSPHERIC AEROSOL CYCLE

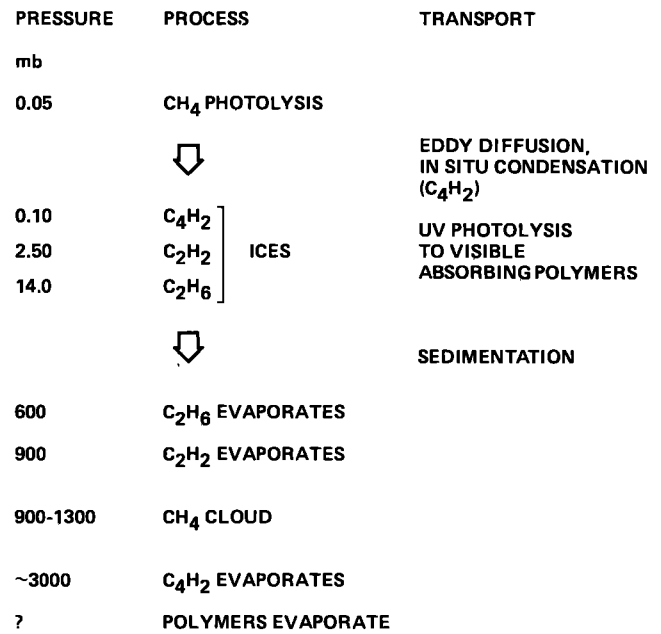| PRESSURE mb	PROCESS	TRANSPORT
0.05	CH$_4$ PHOTOLYSIS	
	⇩	EDDY DIFFUSION, IN SITU CONDENSATION (C$_4$H$_2$)
0.10	C$_4$H$_2$ ⎤	UV PHOTOLYSIS
2.50	C$_2$H$_2$ ⎬ ICES	TO VISIBLE
14.0	C$_2$H$_6$ ⎦	ABSORBING POLYMERS
	⇩	SEDIMENTATION
600	C$_2$H$_6$ EVAPORATES	
900	C$_2$H$_2$ EVAPORATES	
900-1300	CH$_4$ CLOUD	
~3000	C$_4$H$_2$ EVAPORATES	
?	POLYMERS EVAPORATE	

Fig. 9.   Schematic diagram of the stratospheric aerosol cycle.

due to both the very large obliquity of Uranus' axis and the nontrivial value of its orbital eccentricity (0.046).

To first approximation, we might expect that there is very little variation in stratospheric aerosol properties with either latitude or season. This conclusion follows from a combination of the small value of τ_d and the large value of τ_e, as compared to τ_0. Thus meridional winds might smooth out horizontal variations in haze properties on a time scale much less than the orbital period. Furthermore, downward diffusion of precursor gases would occur so slowly from their production region to their condensation levels that the haze properties might reflect the annually averaged insolation. Hence, there might be little net loss of the haze on the night-side; i.e., there would be a continual replenishment of ices lost by sedimentation on the nightside by the continued downward diffusion and condensation of gases from above. Note in this regard that the lower-order hydrocarbons of interest are both produced and destroyed by solar UV radiation. Hence, their abundance in the nightside stratosphere is affected only by downward eddy transport.

However, there are both observational and theoretical reasons for believing that the haze is not totally homogeneous around the planet, at least in terms of its optical properties. First, the circulation may be divided into several large cells with there being relatively little communication among cells. If so, horizontal redistribution would occur only over limited latitude bands. However, note that there should be essentially no variation of haze properties with longitude. Second, Lockwood et al. [1983] found that the geometric albedo of Uranus in the visible increased by about 14% from 1962, when the subsolar and subearth points were close to the equator, to 1981, when these points were located close to the pole. This variation is presumably due to variations in haze properties, since the haze particles are the chief absorbers of sunlight in the Uranian atmosphere, according to arguments presented in the previous subsection. In this regard, the relevant compari-
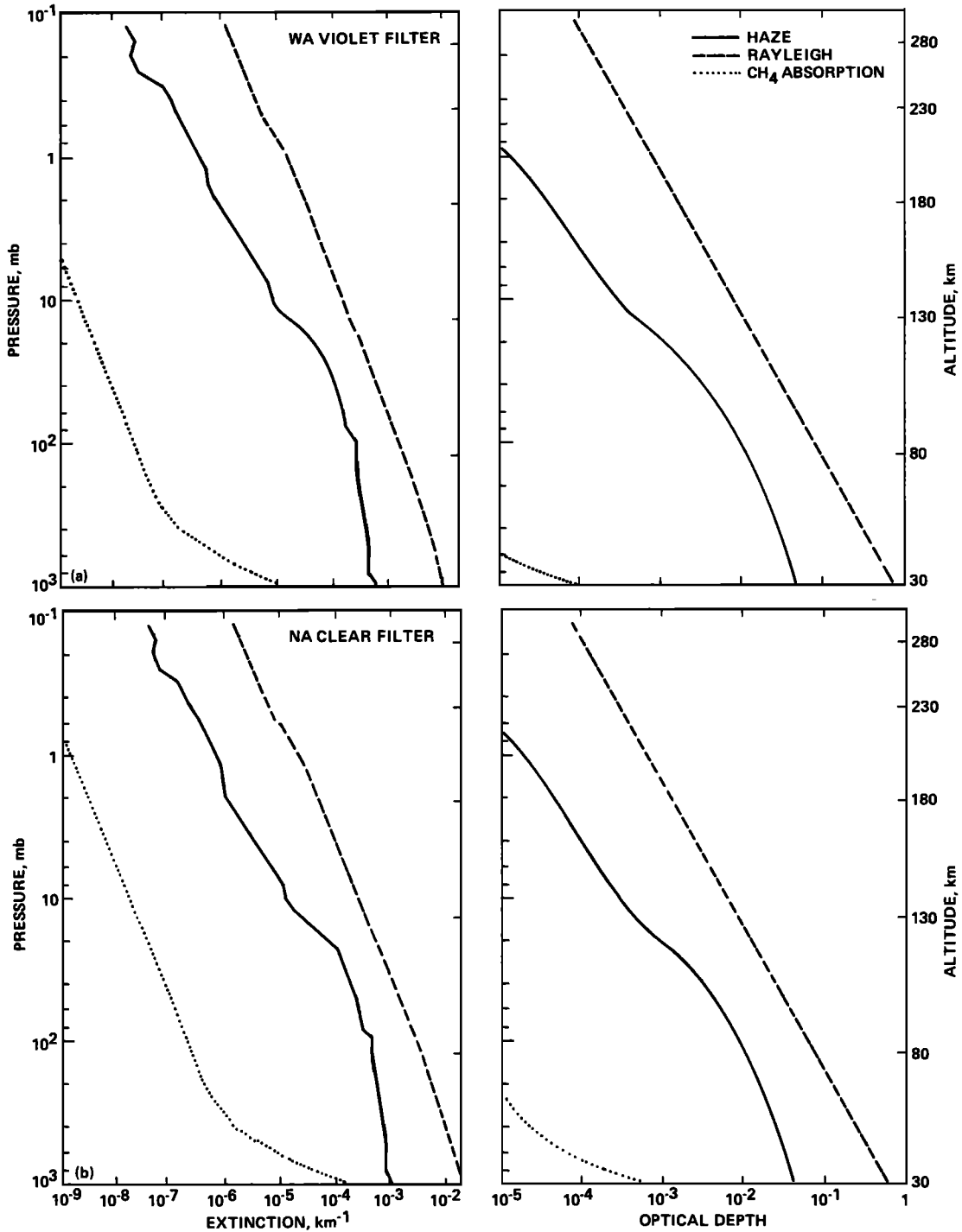
Fig. 10.   Extinction profiles and optical depth as a function of pressure for the low-density solution of model US 8. The solid lines, dashed lines, and dotted lines show the predicted behavior for aerosols, molecular Rayleigh scattering, and gaseous methane absorption, respectively. The calculations have been performed at the effective wavelengths of the following filters of the Voyager wide angle camera: (a) violet, (b) clear, (c) green, (d) orange, (e) short-wavelength methane, and (f) long-wavelength methane.

son is between the fall time scale and the orbital time scale, if UV-induced photolysis of the lower-order hydrocarbon ices produces the visible absorber. According to our earlier discussion, τ_f is smaller than τ_0 at stratospheric altitudes, and hence seasonal variation in the abundance of visible absorbing material is a distinct possibility. Note that the mass of condensed ice need not vary but rather that the amount of UV-produced polymers may vary and hence generate brightness

variations in the visible. In addition, as mentioned above, the amount of condensed diacetylene might vary on a time scale much shorter than an orbital period.

5.   SUMMARY

Figure 9 provides a summary of our current understanding of the stratospheric haze in Uranus' lower stratosphere and upper troposphere. Solar UV photolysis of gaseous methane
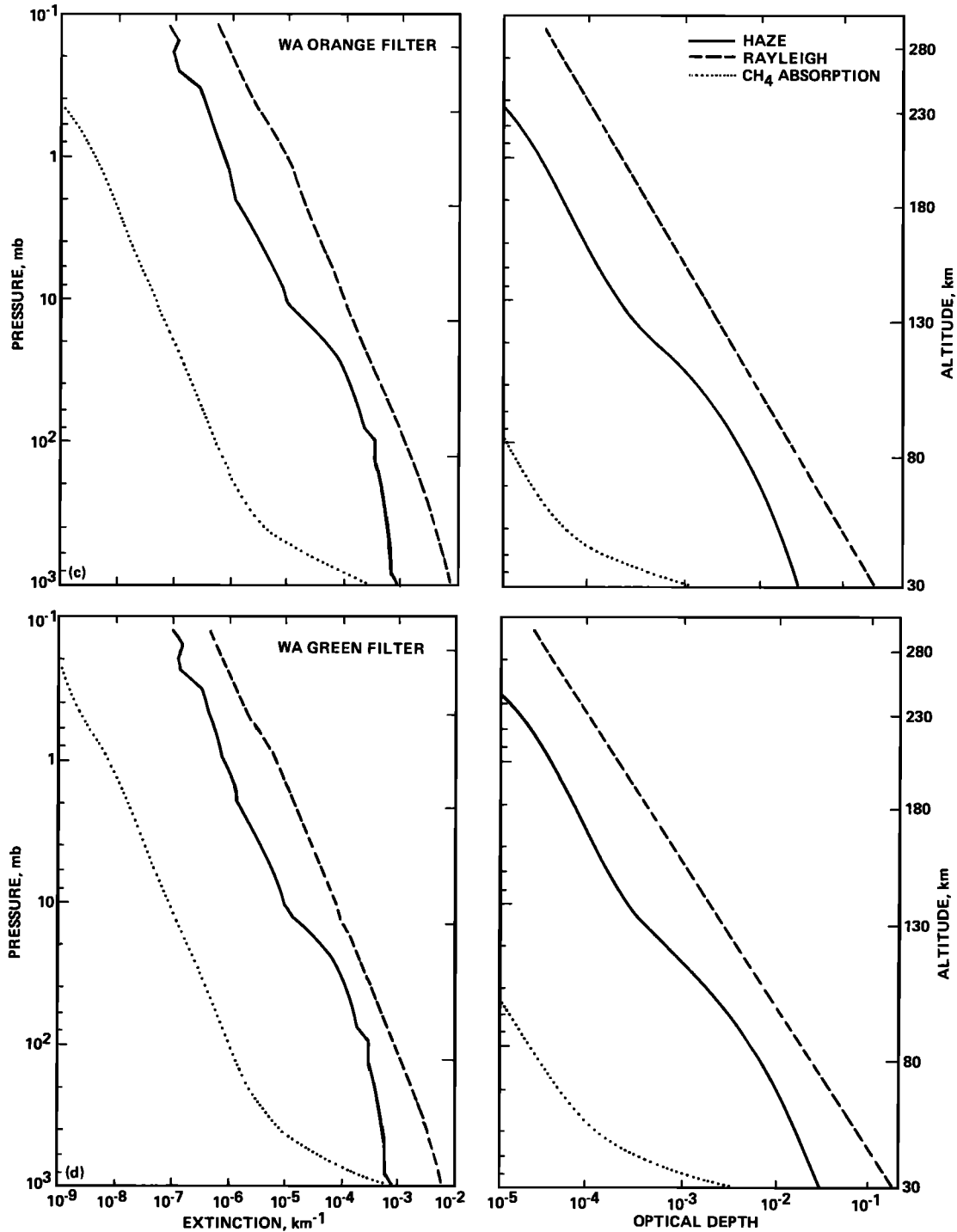
Fig. 10.   (continued)

in the upper stratosphere produces a number of lower-order hydrocarbons including ethane, acetylene, and diacetylene. The latter gases are transported by atmospheric winds of varying scales to the lower stratosphere, where the temperatures are cold enough for them to condense into ices (cf. Figure 1). In particular, diacetylene, acetylene, and ethane are expected to begin condensing at pressure levels of about 0.1, 2.5, and 14 mbar, respectively. In addition, in situ production and condensation of gaseous diacetylene is probably quite important. Almost complete condensation is expected to take place in less

than an atmospheric scale height. Further chemistry may take place as the result of UV radiation acting on these ices. Such solid state chemistry may be an important source of the visible absorbers in Uranus' atmosphere. Aerosols produced by the precipitation of magnetospheric electrons in the auroral zones constitute an additional and possibly important source of visible absorbing material.

For the low-density models that fit the high phase angle, wide-angle images, the stratospheric particles have a modal particle radius of 0.13 ± 0.02 μm and a number density of
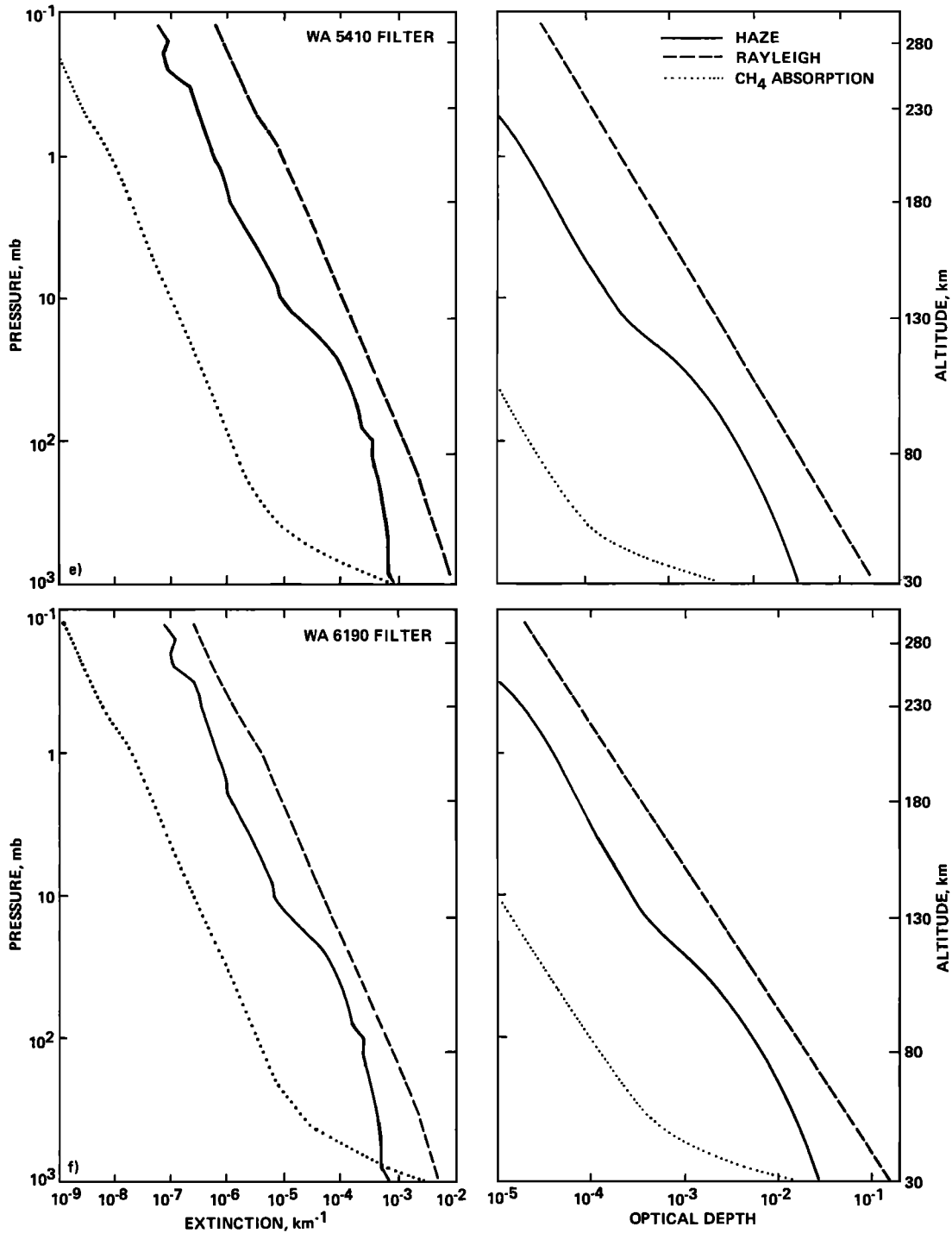
Fig. 10.   (continued)

2 ± 1 particles/cm³ at a reference level of 44 mbar. These values are typical of photochemically produced hazes in other planetary atmospheres [e.g., *Toon and Farlow*, 1981; *West et al.*, 1986]. The modal size steadily increases toward higher pressures; the number density is nearly constant between a few tens and several hundred millibars, it increases steeply to a peak at a few tenths of a millibar, near the diacetylene homogeneous nucleation zone, and it decreases at the highest pressures, owing to continued coagulation and evaporation (cf. Figure 4). Ethane, acetylene, and diacetylene ices are expected

to totally evaporate at pressure levels of approximately 600, 900, and 3000 mbar, respectively.

From a combination of radiative transfer simulations of the Voyager data and a microphysical model of aerosol formation and growth, we infer a total aerosol mass production rate of 2 to 15×10^{-17} g/cm²/s for low-density solutions and a rate that is a factor of 10 larger for high-density solutions. The low-density values are compatible with the rates expected from the photochemical model, while the high-density values are not. Thus the low-density solutions support the assump-

tion that hydrocarbon ices are the dominant source of the stratospheric haze. The predicted vertical profile of the haze scattering parameter defined in Appendix B is consistent with the profile derived from narrow-angle limb images for models having at least half the hydrocarbon ice production being due to the condensation of diacetylene and acetylene. The enhanced ice production aloft, in contrast to the predictions of the nominal photochemical model of Table 2, is attributed to a combination of model uncertainties and the concurrent production and condensation of diacetylene gas. However, the effects of large-scale, vertical winds on these conclusions need to be studied. Additional, albeit weaker support for the hydrocarbon ice model is given by the behavior of the Voyager radio occultation temperature profiles.

The sensitivity of the vertical profiles of the haze-scattering parameter to the relative production rates of the various hydrocarbon ices may be understood in the following way. At pressures less than 10–20 mbar the modal particle size is small compared to a wavelength, and hence the haze-scattering parameter depends on the size to a large power here (up to the sixth power, characterizing Rayleigh scattering). The radiances measured on the wide-angle images tightly constrain the particle size and number density at the reference pressure level of 44 mbar. Throughout much of the lower stratosphere the particles grow chiefly by coagulation, which in turn is determined chiefly by the number density of particles. Given the constraints at 44 mbar, the controlling influence of coagulation on the size of the particles, and the great sensitivity of the haze scattering parameter to size at the lower pressures, the observed profile of this parameter can be reproduced only by having a large enough number density of particles at the lower pressures and therefore a great enough relative production rate at these pressures (it should be recalled that the total production rate is constrained by the wide-angle data).

Figures 10a–10f show the aerosol extinction and optical depth profiles at six visible wavelengths that correspond to the effective wavelengths of five filters of the Voyager wide-angle camera and the clear filter of the narrow-angle camera. These profiles (solid lines) were generated from the best fit to microphysical model US 8. Very similar plots characterize other acceptable models. The dashed and dotted lines in these figures show the corresponding profiles for molecular Rayleigh scattering and gaseous methane absorption, respectively. As can be seen, the extinction coefficient of Rayleigh scattering is larger than that due to the stratospheric haze at all altitudes and wavelengths. Furthermore, the optical depth of the haze in the mid-visible is only about 10^{-2} at the base of the stratosphere and only about a factor of 2 larger at the 600-mbar level, where a major ice species, ethane, is totally evaporated. Thus the key role that this particulate matter plays in the radiative transfer taking place in the lower stratosphere and upper troposphere is the result of its broad continuum absorption in the visible. In this regard, even small decreases in the single-scattering albedo from unity can have dramatic effects on the radiation field.

APPENDIX A: LIMB-VIEWING GEOMETRY: INCLUSION OF PLANET-SCATTERED LIGHT IN THE SOURCE TERM

For a planet such as Uranus, which is fairly bright at the wavelengths of interest, the total light scattered upward from the planet may be comparable in magnitude to the direct solar flux. Furthermore, the scatterers in Uranus' stratosphere are not strongly forward scattering, so light reflected upward from the deeper atmosphere and scattered through intermediate or large scattering angles may be comparable to direct solar il-

lumination scattered through phase angles of 20°–30°. So even when the atmosphere along the line of sight is optically thin, multiply-scattered light may still constitute an appreciable fraction of the total. Therefore we have modified the formalism of *Rages and Pollack* [1983] to include planet-reflected light as well as direct solar illumination in the source term for light scattered in limb-viewing geometries. Below we present a derivation of this added term in the source function and the resultant term in the observed intensity.

The situation is illustrated in Figure A1. Incoming sunlight is scattered off the $\tau = 1$ surface at point S. It then travels to a point Q in the optically thin part of the atmosphere, where it is scattered toward the observer. The geometry of the scattering at S is defined by μ_0, the cosine of the zenith angle of the incoming sunlight, μ'', the cosine of the zenith angle of the outgoing ray, and ϕ', the azimuth angle of the outgoing ray. The geometry of the scattering at Q is defined by $+\mu'$, the cosine of the zenith angle of the incoming ray, μ, the cosine of the zenith angle of the outgoing ray, and the azimuth angle ϕ. For a plane parallel atmosphere, μ'' would be equal to $-\mu'$.

The total multiple-scattering source term at point Q is given by

$$S_m(Q) = 0.25\varpi_0 \int_0^{2\pi} \int_{-1}^{h} R(\mu_0, \mu'', \phi')P(\mu', \mu, \phi) \, d\mu' \, d\phi \quad (10)$$

where

$$h = -(1 - r_1^2/r_Q^2)^{1/2}$$

r_1 is the radius of the $\tau = 1$ surface, and r_Q is the radius of point Q. R is the scattering matrix for the optically thick atmosphere, represented in this case as an $8 \times 8 \times 25$ (μ'', μ_0, and Fourier coefficients in azimuth) matrix derived using an adding-doubling algorithm in a plane parallel atmosphere. Also, ϖ_0 is the haze single-scattering albedo, $P(\theta)$ is the single-scattering phase function at the scattering angle θ, and θ is a function of μ', μ, and ϕ.
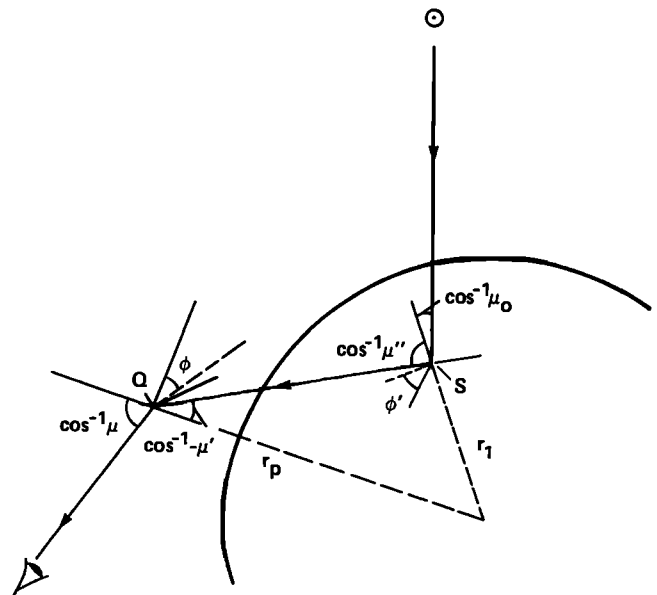

Fig. A1. Geometry of light scattered near the planet's limb. Incident sunlight is reflected from the optically thick part of the atmosphere at point S and travels to point Q above the limb in the optically thin part of the atmosphere, where it is scattered by aerosols and molecules at point Q to the observer.

Figure A2 shows a typical set of results for four different lines of sight above the $\tau = 1$ surface. The horizontal axis is in units of distance along the line of sight from the point at which it is tangent to a spherical surface z (z increases going away from the observer), divided by the impact parameter of the line of sight R_{los}. For purposes of this calculation the planet is assumed to be spherical (polar flattening is ignored). These results were obtained through numerical integration using four-point Gaussian quadrature in μ' and Simpson's rule with 45° intervals in ϕ.

The magnitudes of the multiple-scattering source terms for these viewing geometries are around 40% of the single-scattering source term for the same viewing geometry. While the exact value of S_m increases as the line of sight is moved lower, the magnitude of the variation is only about 10% of the total. Therefore the multiple-scattering source term found for an impact parameter of 25,600 km (100 km above the $\tau = 1$ surface) will be used at all other altitudes as well. The computations will be further simplified by assuming that S_m as a function of z consists of two linear segments, one for $z < 0$ and the other for $z > 0$.

Consider an atmosphere consisting of concentric spherical shells numbered consecutively beginning with the outermost (Figure 8 [Rages and Pollack, 1983]). The inner boundary of layer j is labeled r_j, and the extinction coefficient of layer j (in units of km^{-1}) is defined as β_j. Now consider a line of sight which is tangent to a spherical shell at a radius r_n. This line of sight can be divided into $2n$ segments, since it will pass through each of the n outermost shells twice. Within each of these $2n$ segments the specific intensity I_n/F_m can be calculated analytically. The total can then be found by summing the results for all the segments.

For segment i of this line of sight the index of the corresponding spherical shell is

$$j = i \qquad i \le n$$
$$j = 2n + 1 - i \qquad i > n \tag{11}$$

Also, the point at which the line of sight intersects the boundary of segment i furthest from the observer is

$$z_i = -(r_i^2 - r_n^2)^{1/2} \qquad i \le n$$
$$z_i = (r_{2n-i}^2 - r_n^2)^{1/2} \qquad i > n \tag{12}$$

$\Delta z_i = z_i - z_{i-1}$, and the value of the multiple-scattering source term is $S_m = S_0 + z\delta S$, where

$$\delta S = \delta S_- \qquad i \le n$$
$$\delta S = \delta S_+ \qquad i > n \tag{13}$$

Then

$$I_i/F_m = \int_{z_{i-1}}^{z_i} e^{-\tau(z'')} S_m \beta_j \, dz'' \tag{14}$$

where $\tau(z'')$ is the optical depth along the outgoing ray path from z'' to $-\infty$. Making the transformations $z' = z'' - z_{i-1}$ and $\tau(z') = \tau_0 + \beta_j z'$, where τ_0 is evaluated at z_{i-1},

$$I_i/F_m = e^{-\tau_0} \int_0^{\Delta z_i} (S_0 \, \delta S z_{i-1} + \delta S z') \exp(-\beta_j z')\beta_j \, dz' \tag{15}$$

Carrying out the integration leads to

$$I_i/F_m = e^{-\tau_0} \{[S_0 + \delta S(z_i + \beta_j^{-1})]$$
$$\cdot [1 - \exp(-\beta_j \Delta z_i)] - \delta S \Delta z_i\} \tag{16}$$

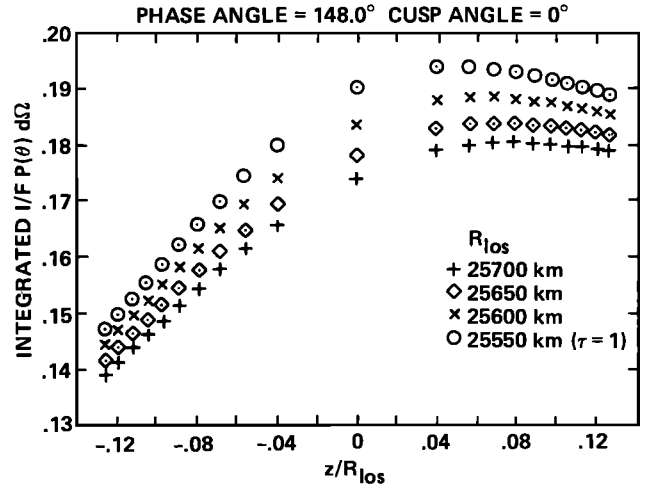The total multiple-scattering contribution to the specific in-

Fig. A2. Magnitude of the source term for planet-reflected light (ordinate) that is scattered in the optically thin part of the atmosphere as a function of distance z from the tangent point for the line of sight (abscissa). In this figure, distance z is normalized by the distance of the tangent point from the planet's center, R_{los}. Results are shown for four choices of R_{los}. The optical depth of the atmosphere (for normal incidence) is unity at R_{los} equal to 25,550 km.

tensity is

$$I/F_m = \sum_{i=1}^{2n} I_n/F_m \tag{17}$$

For Uranus this usually amounts to about a third of the specific intensity due to the single scattering of incoming sunlight at a phase angle of 157° and to about 40–50% of the single-scattering term at a phase angle of 148°.

APPENDIX B: LIMB-VIEWING GEOMETRY: DETERMINATION OF THE HAZE SCATTERING PARAMETER

The limb inversion uses measurements of I/F, the specific intensity of light scattered through a particular phase angle by the atmosphere, as a function of altitude. If the slant optical depth along a line of sight is less than unity, I/F is dominated by the contribution of the innermost spherical shell encountered by the line of sight. One reason for this is that in general the extinction per kilometer β declines rapidly with increasing altitude. A more significant factor is the length of the path through the innermost layer, which is much greater than the path lengths through any of the higher layers. (For Uranus a typical impact parameter is 25,600 km. If each spherical layer is 10 km thick, the path length through the innermost layer (25,610 km to 25,600 km) is 716 km. The path length through the next-lowest layer (25,620 km to 25,610 km) is 297 km.)

Inversion of the limb profile of I/F, with due allowance for the planet-reflected component (see Appendix A), leads to a vertical profile of the total extinction coefficient $\beta_{n,tot}$ and a determination of the product of the total single-scattering albedo $\varpi_{0n,tot}$ and phase function $P_{n,tot}(\theta)$. This product is assumed to be independent of altitude for the purpose of the inversion. The term "total" refers to the combined effects of gas molecules and aerosols in interacting with light. Below, we use the dominance of the observed I/F by the innermost spherical shell at slant path optical depths less than unity to achieve a separation of the molecular and aerosol components

of the quantities derived by the inversion technique and hence isolate a component, which we term the "haze scattering parameter," that depends only on the properties of the haze. Thus we are able to derive a vertical profile of the haze scattering parameter from the limb inversion. This profile can be compared with those predicted by various microphysical models to help assess their validity.

Assuming negligible attenuation of the incoming and scattered light in the overlying atmosphere, the specific intensity due to single scattering along a line of sight which is tangent to a spherical shell at r_n is

$$I_n/F_s = 0.25\varpi_{0n,\text{tot}}P_{n,\text{tot}}(\theta)\{1 - \exp[-2z_{n-1}(\beta_{n,\text{tot}} + \gamma_n)]\} \quad (18)$$

where γ_n is the change in optical depth along the incoming ray path divided by z_{n-1} (see Equation 5 of *Rages and Pollack* [1983]). In the Voyager continuum filters, methane absorption is negligible in Uranus' stratosphere, so

$$\beta_{n,\text{tot}} = \beta_{n,\text{haz}} + \beta_{n,\text{Ray}} \quad (19)$$

$$\varpi_{0n,\text{tot}}P_{n,\text{tot}}(\theta) = \frac{1}{\beta_{n,\text{tot}}} (\beta_{n,\text{haz}}\varpi_{0n,\text{haz}}P_{n,\text{haz}}(\theta) + \beta_{n,\text{Ray}}\varpi_{0n,\text{Ram}}P_{n,\text{Ray}}(\theta)) \quad (20)$$

where the subscript haz refers to the stratospheric haze particles and Ray to molecular Rayleigh scattering, and $\varpi_{0n,\text{Ram}}$ is the Raman scattering albedo.

Unless the solar phase angle is very close to 180°, γ_n will be much less than $\beta_{n,\text{tot}}$, and (18) can be rewritten as

$$I_n/F_s = 0.25\varpi_{0n,\text{tot}}P_{n,\text{tot}}(\theta)[1 - \exp(-2z_{n-1}\beta_{n,\text{tot}})] \quad (21)$$

or for the case of an optically thin line of sight,

$$I_n/F_s = 0.5z_{n-1}\varpi_{0n,\text{tot}}P_{n,\text{tot}}(\theta)\beta_{n,\text{tot}} \quad (22)$$

In addition to singly scattered sunlight there is light reflected from the deeper parts of the atmosphere, which is then scattered one final time in the optically thin stratosphere. For the innermost layer along an optically thin line of sight this component of the outgoing specific intensity is

$$I_n/F_m = S_0[1 - \exp(-2\beta_{n,\text{tot}}z_{n-1})] = 2\beta_{n,\text{tot}}S_0z_{n-1} \quad (23)$$

$$S_0 = 0.25\varpi_{0n,\text{tot}}\int_0^{2\pi}\int_{-1}^h R(\mu_0, \mu'', \phi')P_{n,\text{tot}}(\mu', \mu, \phi) \, d\mu' \, d\phi$$

$$= \frac{0.25}{\beta_{n,\text{tot}}}\left[\beta_{n,\text{haz}}\varpi_{0n,\text{haz}}\int_0^{2\pi}\int_h^1 R(\mu_0, \mu'', \phi')\right.$$

$$\cdot P_{n,\text{haz}}(\mu', \mu, \phi) \, d\mu' \, d\phi$$

$$+ \beta_{b,\text{Ray}}\varpi_{0n,\text{Ram}}\int_0^{2\pi}\int_h^1 R(\mu_0, \mu'', \phi')$$

$$\cdot P_{n,\text{Ray}}(\mu', \mu, \phi) \, d\mu' \, d\phi \quad (24)$$

If C_{tot} is defined as

$$C_{\text{tot}} = \frac{1}{P_{n,\text{tot}}(\theta)}\int_0^{2\pi}\int_{-1}^h R(\mu_0, \mu'', \phi')P_{n,\text{tot}}(\mu', \mu, \phi) \, d\mu' \, d\phi \quad (25)$$

and C_{haz} and C_{Ray} are similarly defined, then (24) becomes

$$S_0 = 0.25\varpi_{0n,\text{tot}}P_{n,\text{tot}}(\theta)C_{\text{tot}} = \frac{0.25}{\beta_{n,\text{tot}}}(\beta_{n,\text{haz}}\varpi_{0n,\text{haz}}P_{n,\text{haz}}(\theta)C_{\text{haz}}$$

$$+ \beta_{n,\text{Ray}}\varpi_{0n,\text{Ram}}P_{n,\text{Ray}}(\theta)C_{\text{Ray}}) \quad (26)$$

and substituting in (23) gives

$$I_n/F_m = 0.5z_{n-1}(\beta_{n,\text{haz}}\varpi_{0n,\text{haz}}P_{n,\text{haz}}(\theta)C_{\text{haz}}$$

$$+ \beta_{n,\text{Ray}}\varpi_{0n,\text{Ram}}P_{n,\text{Ray}}(\theta)C_{\text{Ray}}) \quad (27)$$

The total specific intensity along an optically thin line of sight is then obtained by adding together (22) and (27):

$$I_n/F = 0.5z_{n-1}\beta_{n,\text{tot}}\varpi_{0n,\text{tot}}P_{n,\text{tot}}(\theta)(1 + C_{\text{tot}})$$

$$= 0.5z_{n-1}[\beta_{n,\text{haz}}\varpi_{0n,\text{haz}}P_{n,\text{haz}}(\theta)(1 + C_{\text{haz}})$$

$$+ \beta_{n,\text{Ray}}\varpi_{0n,\text{Ram}}P_{n,\text{Ray}}(\theta)(1 + C_{\text{Ray}})] \quad (28)$$

or

$$\beta_{n,\text{haz}}\varpi_{0n,\text{haz}}P_{n,\text{haz}}(\theta)(1 + C_{\text{haz}})$$

$$= \frac{I_n/F}{0.5z_{n-1}} - \beta_{n,\text{Ray}}\varpi_{0n,\text{Ram}}P_{n,\text{Ray}}(\theta)(1 + C_{\text{Ray}}) \quad (29)$$

The left-hand side of this equation is the definition of "haze scattering parameter." It can be evaluated in a straightforward manner for a given microphysical model. The right-hand side of the equation gives a prescription for deriving the haze scattering parameter from a limb inversion. The parameter C_{Ray} was evaluated by using the standard microphysical model UF 10 in the plane parallel, multiple-scattering code to define the quantity R. The values of C_{Ray} so found should be almost identical for the other microphysical models of interest.

REFERENCES

Atreya, S. K., Eddy mixing coefficient on Saturn, *Planet. Space Sci.*, *30*, 849–854, 1982.

Atreya, S. K., Aeronomy in Uranus and Neptune, *NASA Spec. Publ.*, SP-2330, 55–88, 1984.

Atreya, S. K., and J. J. Ponthreu, Photolysis of methane and the ionosphere of Uranus, *Planet. Space Sci.*, *31*, 939–944, 1983.

Atreya, S. K., and P. N. Romani, Photochemistry and clouds of Jupiter, Saturn, and Uranus, in *Recent Advances in Planetary Meteorology*, edited by G. E. Hunt, pp. 17–68, Cambridge University Press, New York, 1985.

Atreya, S. K., T. M. Donahue, and M. C. Festou, Jupiter: Structure and composition of the upper atmosphere, *Astrophys. J.*, *247*, 143–47, 1981.

Atreya, S. K., B. K. Sandel, P. N. Romani, F. Herbert, A. L. Broadfoot, and R. V. Yvelle, Voyager/Uranus UV occultations: Atmospheric vertical mixing and photochemistry, *Bull. Am. Astron. Soc.*, *18*, 758, 1986.

Baines, K. H., and J. T. Bergstralh, The structure of the Uranian atmosphere: Constraints from the geometric albedo spectrum and H_2 and CH_4 line profiles, *Icarus*, *65*, 406–441, 1986.

Chemical Rubber Company, *Handbook of Chemistry and Physics*, Cleveland, Ohio, 1975.

Danielson, G. E., P. N. Kupferman, T. V. Johnson, and L. A. Soderblom, Radiometric performance of the Voyager cameras, *J. Geophys. Res.*, *86*, 8683–8689, 1981.

Donnay, *Crystal Data Determination Tables*, 3rd Ed., vol. 1, U.S. Department of Commerce, Washington, D. C., 1972.

Elliot, J. L., R. G. French, J. A. Frogel, J. H. Elias, D. M. Mink, and W. Liller, Orbits of nine Uranian rings, *Astron. J.*, *86*, 444–455, 1981.

Esposito, L. W., R. G. Knollenberg, M. Ya. Marov, O. B. Toon, and R. P. Turco, The clouds and hazes of Venus, in *Venus*, edited by D. M. Hunten, L. Colin, T. M. Donahue, and V. I. Moroz, pp. 484–564, University of Arizona Press, Tucson, 1983.

Fleagle, R. G., and J. A. Businger, *An Introduction to Atmospheric Physics*, Academic, Orlando, Fla., 1963.

Fuchs, N. A., *The Mechanics of Aerosols*, Pergamon, New York, 1964.

Glicker, S., and H. Okabe, Photochemistry of diacetylene, *J. Phys. Chem.*, *91*, 437–440, 1987.

Hanel, R., et al., Infrared observations of the Uranian system, *Science*, *233*, 70–74, 1986.

Hansen, J. E., and L. D. Travis, Light scattering in planetary atmospheres, *Space Sci. Rev.*, *16*, 527–610, 1974.

Herbert, F., B. R. Sandel, R. V. Yelle, J. B. Holberg, A. L. Broadfoot, D. E. Shemansky, S. K. Atreya, and P. N. Romani, The upper atmosphere of Uranus: EUV occultations observed by Voyager 2, *J. Geophys. Res.*, this issue.

Kasten, F., Falling speed of aerosol particles, *J. Appl. Meteorol.*, *7*, 944–947, 1968.

Khare, B. N., C. Sagan, W. R. Thompson, E. T. Arakawa, and P. Votaw, Solid hydrocarbon aerosols produced in simulated Uranian and Neptunian stratospheres, *J. Geophys. Res.*, this issue.

Lane, A. L., et al., Photometry from Voyager 2: Initial results from the Uranian atmosphere, satellites, and rings, *Science*, *233*, 65–70, 1986.

Lindal, G. F., J. R. Lyons, D. N. Sweetnam, V. R. Eshleman, D. P. Hinson, and G. L. Tyler, The atmosphere of Uranus: Results of radio occultation measurements with Voyager 2, *J. Geophys. Res.*, this issue.

Lockwood, G. W., B. L. Lutz, D. T. Thompson, and A. Warnock, III, The albedo of Uranus, *Astrophys. J.*, *266*, 402–414, 1983.

Lombos, B. A., P. Sauvageau, and C. Sandorfy, Far ultraviolet spectra of solid films of methane, ethane, and propane, *Chem. Phys. Lett.*, *1*, 382–384, 1967.

Neff, J. S., D. C. Humm, J. T. Bergstralh, A. L. Cochran, W. D. Cochran, E. S. Barker, and R. G. Tull, Absolute spectrophotometry of Titan, Uranus, and Neptune: 3500–10,500 A, *Icarus*, *60*, 221–235, 1984.

Noy, N., M. Podolak, and A. Bar-Nun, Acetylene photopolymers in Jupiter's atmosphere, *Icarus*, *40*, 199–204, 1979.

Podolak, M., A. Bar-Nun, N. Noy, and L. Giver, Inhomogeneous models of Titan's aerosol distribution, *Icarus*, *57*, 72–82, 1984.

Pollack, J. B., and J. N. Cuzzi, Scattering by nonspherical particles of size comparable to a wavelength: A new semi-empirical theory and its application to tropospheric aerosols, *J. Atmos. Sci.*, *37*, 868–881, 1980.

Pollack, J. B., K. Rages, K. H. Baines, J. T. Bergstralh, D. Wenkert, and G. E. Danielson, Estimates of the bolometric albedos and radiation balance of Uranus and Neptune, *Icarus*, *65*, 442–466, 1986a.

Pollack, J. B., C. Stoker, K. Rages, M. Tomasko, and S. Pope, Cloud structure in Uranus' atmosphere based on Voyager imaging observations, *Bull. Am. Astron. Soc.*, *18*, 757, 1986b.

Rages, K., and J. B. Pollack, Vertical distribution of scattering hazes in Titan's upper atmosphere, *Icarus*, *55*, 50–62, 1983.

Rages, K., J. B. Pollack, and P. H. Smith, Size estimates of Titan's aerosols based on Voyager high-phase-angle images, *J. Geophys. Res.*, *88*, 8721–8728, 1983.

Romani, P. N., and S. K. Atreya, Polyacetylene photochemistry production and condensation on Uranus, *Bull. Am. Astron. Soc.*, *18*, 758, 1986.

Smith, B. A., et al., Voyager 2 in the Uranian system: Imaging science results, *Science*, *233*, 43–64, 1986.

Smith, P. H., and M. G. Tomasko, Photometry and polarimetry of Jupiter at high phase angles, *Icarus*, *58*, 35–73, 1984.

Stief, L. J., V. J. DeCarlo, and R. J. Mataloni, Vacuum-ultraviolet photolysis of acetylene, *J. Chem. Phys.*, *42*, 3113–3121, 1965.

Stull, D. R., Vapor pressure of pure substances: Organic compounds, *Ind. Eng. Chem.*, *39*, 517–540, 1947.

Thompson, W. R., T. Henry, B. N. Khare, L. Flynn, J. Schwartz, and C. Sagan, Light hydrocarbons from plasma discharge in $H_2/He/CH_4$: First results and Uranian auroral chemistry, *J. Geophys. Res.*, this issue.

Tomasko, M. G., and L. R. Doose, Polarimetry and photometry of Saturn from Pioneer 11: Observations and constraints on the distribution and properties of cloud and aerosol particles, *Icarus*, *58*, 1–34, 1984.

Toon, O. B., and N. H. Farlow, Particles above the tropopause: Measurements and models of stratospheric aerosols, meteoritic debris, nacreous clouds, and noctilucent clouds, *Annu. Rev. Earth Planet. Sci.*, *9*, 19–58, 1981.

Toon, O. B., R. P. Turco, and J. B. Pollack, A physical model of Titan's clouds, *Icarus*, *43*, 260–282, 1980.

Tyler, G. L., et al., Voyager 2 radio science observations of the Uranian system: Atmosphere, rings, and satellites, *Science*, *233*, 79–84, 1986.

Vogel, A. I., Physical properties and chemical constituents, XXIII, Miscellaneous compounds, *J. Chem. Soc.*, 1833–1855, 1948.

Wagener, R., J. Caldwell, and K. Fricke, The geometric albedos of Uranus and Neptune between 2100 and 3350 A, *Icarus*, *67*, 281–288, 1986.

Wallach, D., and B. Hapke, Light scattering in a spherical, exponential atmosphere, with application to Venus, *Icarus*, *63*, 354–373, 1985.

West, R. A., D. F. Strobel, and M. G. Tomasko, Clouds, aerosols, and photochemistry in the Jovian atmosphere, *Icarus*, *65*, 161–217, 1986.

Yung, Y. L., M. Allen, and J. P. Pinto, Photochemistry of the atmosphere of Titan: Comparison between model and observations, *Astrophys. J.*, *55*, 465–506, 1984.

Ziegler, W. T., The vapor pressures of some hydrocarbons in the liquid and solid state at low temperatures, *NBS Tech. Note U.S.*, *4*, 1959.

Ziegler, W. T., B. S. Kirk, J. C. Mullins, and A. R. Berquist, Calculations of the vapor pressure and heats of sublimation of liquids and solids below one atmosphere pressure, 7, Ethane, *Ga. Inst. Technol. Eng. Exp. Stn. Tech. Rep.*, *2*, 1964.

S. K. Atreya, University of Michigan, Ann Arbor, MI 48109.

J. B. Pollack and K. Rages, NASA Ames Research Center, Moffett Field, CA 94035.

S. K. Pope and G. Tomasko, University of Arizona, Tucson, AZ 85721.

P. N. Romani, Code 695, NASA Goddard Space Flight Center, Greenbelt, MD 20771.